ACS APPLIED MATERIALS & INTERFACES

www.acsami.org

Research Article

Understanding Multi-Ion Transport Mechanisms in Bipolar Membranes

Justin C. Bui, Ibadillah Digdaya, Chengxiang Xiang, Alexis T. Bell, and Adam Z. Weber*

Cite This: *ACS Appl. Mater. Interfaces* 2020, 12, 52509–52526

Read Online

ACCESS | Metrics & More | Article Recommendations | Supporting Information

ABSTRACT: Bipolar membranes (BPMs) have the potential to become critical components in electrochemical devices for a variety of electrolysis and electrosynthesis applications. Because they can operate under large pH gradients, BPMs enable favorable environments for electrocatalysis at the individual electrodes. Critical to the implementation of BPMs in these devices is understanding the kinetics of water dissociation that occurs within the BPM as well as the co- and counter-ion crossover through the BPM, which both present significant obstacles to developing efficient and stable BPM-electrolyzers. In this study, a continuum model of multi-ion transport in a BPM is developed and fit to experimental data. Specifically, concentration profiles are determined for all ionic species, and the importance of a water-dissociation catalyst is demonstrated. The model describes internal concentration polarization and co- and counter-ion crossover in BPMs, determining the mode of transport for ions within the BPM and revealing the significance of salt-ion crossover when operated with pH gradients relevant to electrolysis and electrosynthesis. Finally, a sensitivity analysis reveals that the performance and lifetime of BPMs can be improved substantially by using of thinner dissociation catalysts, managing water transport, modulating the thickness of the individual layers in the BPM to control salt-ion crossover, and increasing the ion-exchange capacity of the ion-exchange layers in order to amplify the water-dissociation kinetics at the interface.

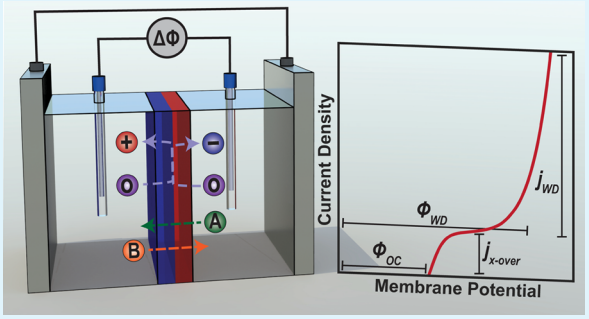

KEYWORDS: *bipolar membrane, transport, model, electrochemistry, ionomers, electrolysis, CO_2 reduction, water splitting*

1. INTRODUCTION

As electricity from renewable sources becomes less expensive and more prevalent, the electrochemical conversion of low-value feedstocks to high-value products (electrolysis or electrosynthesis) will become a key means for storing excess electrical energy in chemical carriers, simultaneously offsetting the intermittency of renewable energy sources and decarbonizing various sectors of the economy.[1,2] For many electrolysis or electrosynthesis reactions, the optimal device configuration would enable operation under an applied pH gradient, where the anode catalyst is immersed in a drastically different pH environment than the cathode catalyst.[3−6]

Consider the electrolysis of water to hydrogen (H_2) and oxygen (O_2)—a relatively simple electrochemical reaction that has been heavily studied due to hydrogen's particular attractiveness as a fuel alternative for a wide range of applications.[7] In a water electrolyzer, the hydrogen-evolution reaction (HER) and oxygen-evolution reaction (OER) occur at the cathode and anode, respectively. It is often true that optimal conditions for the desired OER catalyst occur in a drastically different environment than that for the HER catalyst. For example, platinum (Pt), the state-of-the-art cathode material, exhibits higher activity in acidic environments than in alkaline environments.[8] Conversely, practically all low-overpotential, earth-abundant OER catalysts are only stable in alkaline environments.[8] Currently, electrolyzers circumvent the stability issue by using expensive iridium or iridium oxide catalysts that can withstand acidic environments.[8] However, it would be preferable to operate in an alkaline environment in order to facilitate usage of more affordable transition metal catalysts that possess higher OER activities than iridium-based catalysts.[7] Therefore, the optimal configuration for a water electrolyzer would be one in which the cathode is at an acidic pH, while the anode is simultaneously maintained at an alkaline pH.

A similar behavior can be observed for other electrochemical processes. For instance, electrochemical CO_2 reduction[6] and ammonia synthesis[9] would benefit from use of a BPM under an applied pH gradient of pH 7 at the cathode and pH 14 at the anode. This differs slightly from the pH 0-14 gradient optimal for water electrolysis, with the pH 7 chosen at the cathode to

Received: July 14, 2020
Accepted: October 23, 2020
Published: November 10, 2020

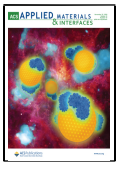

https://dx.doi.org/10.1021/acsami.0c12686
ACS Appl. Mater. Interfaces 2020, 12, 52509−52526

decrease HER selectivity. The benefits derived from operation under pH gradients even extend to the field of organic electrosynthesis; the cathodic organic electrosynthesis reaction of acrylonitrile to adiponitrile is most selective in near neutral pHs (~pH 7) due to solubility concerns of the organic reagents and selectivity concerns with HER[10,11] and would most desirably be paired with an oxygen evolving anode at pH 14. For methane oxidation, an applied pH gradient of pH 0-7 would be beneficial to pair efficient HER at the cathode with the near neutral environments of the organic reagents at the anode.[12] Nonetheless, pH 7-7 operation is still relevant for solar-driven water splitting or seawater electrolysis applications.[13]

The pH gradients desired for water electrolysis and similar electrochemical reactions cannot be feasibly maintained in the uniform pH environments of current electrolyzers. While the pH gradient could be maintained by a constant flow of electrolyte on either side of the device, this is less practical because of the amount of electrolyte required. However, by implementing a bipolar membrane (BPM), composed of a cation-exchange layer (CEL) and an anion-exchange layer (AEL) laminated together, it becomes possible to maintain a pH gradient across the device and enable optimal conditions for the catalysis of both half reactions.[4,14−19]

A BPM is shown schematically in Figure 1. The CEL contains negative fixed-charge groups, such as sulfonate anions

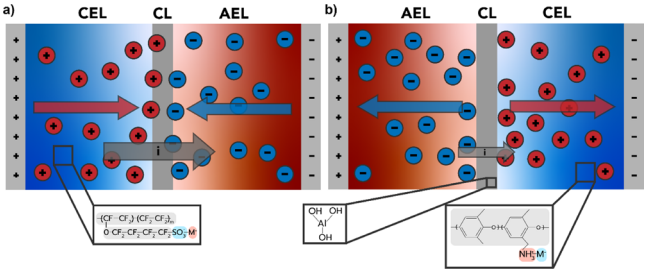

Figure 1. Schematic of a bipolar membrane with a cation-exchange layer, an anion-exchange layer, and a catalyst layer in (a) forward and (b) reverse bias. As depicted in the insets, the CEL contains sulfonate negative fixed-charge groups, the AEL contains quaternary ammonium positive fixed-charge groups, and the water-dissociation catalyst is $Al(OH)_3$. It is noted, though, that any combination of CEL, AEL, and water-dissociation catalyst chemistries can be used in the BPM. In the forward bias case, current (gray arrow) is driven by water recombination. For reverse bias, current is driven by water dissociation.

($-SO_3^-$). The high concentration of negative fixed-charge groups ameliorates anion uptake in the CEL due to Donnan exclusion, diminishing anionic transport due to their low concentration in the CEL and thus enabling high selectivity to cation transport.[20,21] Conversely, the AEL contains positive fixed-charge groups, such as quaternary ammonium cations ($-NH_4^+$), that help to exclude cations in the AEL, limiting cationic transport in the AEL and leading to selective anion transport in the AEL.[22] In some cases, a water-dissociation catalyst layer (CL) is included between the AEL and CEL that contains weakly acidic or basic groups to catalyze the dissociation of water.[23] Various metal oxides,[24] aluminum hydroxide ($Al(OH)_3$),[25] and graphene oxide[19,26,27] have been explored as water-dissociation catalysts.

BPMs have two modes of operation as defined by the direction of the flow of current: reverse bias and forward bias.[28−30] In forward bias (Figure 1a), the CEL side of the BPM is held at high potential and the AEL side is held at low potential. Under this applied potential, the cations in the CEL and the anions in the AEL will both move toward the AEL/CEL interface due to migration, and the hydronium cations and hydroxide anions will form water at the interface, resulting in high recombination rates or current densities due to mass action.[23,28,29]

In reverse bias (Figure 1b), the CEL is held at low potential and the AEL is held at high potential. In this case, the mobile charges in each ion-exchange layer will move away from the junction. This decreases the concentration of mobile ions in the catalyst layer, increasing the resistance of the BPM until a mass-transfer-limited crossover current is achieved.[23,31] However, as the applied potential in a reverse-bias BPM increases, the BPM experiences a "breakdown", at which point the rate of water dissociation is sufficiently amplified by the electric field, and consequently higher current densities are attained.[23,31,32] This phenomenon is known as the Second Wien Effect.[32] A water-dissociation catalyst is used to reduce the free energy of the Bjerrum dipole transition state and thus minimize the applied potential required to achieve breakdown.[33,34] The reverse-bias configuration is preferable for implementation in most electrolysis applications because it optimally pairs the anode with the AEL while simultaneously pairing the cathode with the CEL.[4] Therefore, for this work, the BPM will be considered in the reverse-bias configuration.

A number of experimental studies have utilized BPMs in reverse bias for electrolysis.[18,27,35,36] The electrochemical characteristics of these materials have been widely characterized using four-probe experiments to deconvolute the membrane potential from the kinetic overpotentials at the working electrodes, effectively isolating the interfacial water dissociation. Nonetheless, the phenomena controlling water dissociation in the interfacial catalyst layer are still poorly understood. Furthermore, while there have been some attempts to characterize the effects of ionic salt species, the influence of co- and counter-ion crossover during the operation of reverse-bias BPMs continues to be a subject of discussion.[4,23]

In the study of BPMs, it is tempting to ignore ions other than hydronium (H_3O^+) or hydroxide (OH^-) present in the BPM and study only the dissociation of water. However, the BPM can also uptake salt ions from the electrolyte and these species can transport across the membrane. The salt ions are typically classified as either co-ions (salt ions in the electrolyte with the same charge as the adjacent ion-exchange layer) or counter-ions (salt ions in the electrolyte with opposite charge to the adjacent ion-exchange layer). Mitigating the transport of these co- and counter-ions is vital for developing stable BPM-electrolyzers because excess salt-ion crossover enables mixing of the electrolytes and results in the gradual neutralization of the pH gradient.[5]

Modeling efforts for reverse-bias BPMs attempted to replicate four-probe experiments by solving the Poisson equation locally near the junction[32] or with continuum transport models of the entire BPM based on a modified Poisson−Nernst−Planck formulation that includes the Second Wien Effect.[23,34,37,38] Unfortunately, there is a dearth of studies that have attempted to simulate the electrochemical characteristics of BPMs under the high applied pH gradients relevant to implementation in electrosynthesis devices. Prior models also neglect water concentration gradients within the BPM, which

https://dx.doi.org/10.1021/acsami.0c12686
ACS Appl. Mater. Interfaces 2020, 12, 52509−52526

are critical to driving ion transport within the BPM and can have significant effects on its properties.[20,25]

In this paper, we present a comprehensive model that describes multi-ion transport and interactions, homogeneous reaction kinetics, and water-dissociation catalysis in a reverse-bias-operation BPM under various applied pH gradients and for electrolytes with varying buffer species. The model differs from those reported in prior studies in its treatment of homogeneous buffer kinetics and water uptake and is, to the best of our knowledge, the first to simulate the BPM under conditions relevant to efficient electrolysis and electrosynthesis. By capturing the effects of the aforementioned phenomena, the model explains experimental polarization curves of BPMs in distinct electrolyte environments. The impact of electrolyte species, water uptake, membrane properties, and water-dissociation catalysts are examined in these various pH environments in order to inform future design of high-performance BPMs.

2. COMPUTATIONAL METHODS

This section describes the modeling approach, governing equations, and assumptions with the aim of providing the reader with an understanding of the methodology used to capture the complex physics of multi-ion transport in a reverse-bias BPM. The BPM model employed here is designed to mimic a four-electrode experiment (Figure 2a), where an applied potential is measured between

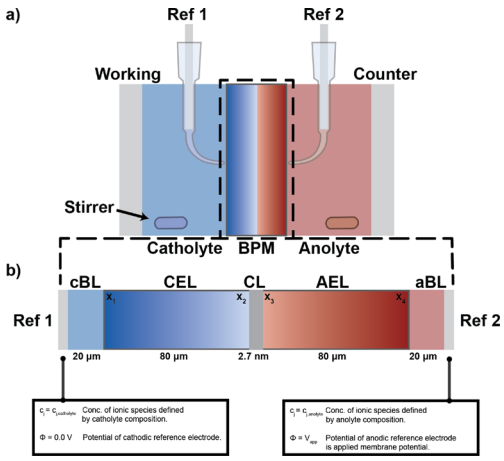

Figure 2. (a) Standard four-probe experimental setup. (b) Schematic representation of model and boundary conditions.

reference electrodes that probe electrostatic potential in close proximity to the two ends of the BPM through the use of Luggin capillaries.[4] By employing a four-electrode experimental setup, the kinetic overpotentials associated with faradaic reactions occurring at the working or counter electrode are separated from the potential drop across the membrane, thereby allowing for isolated measurement of current/voltage characteristics of the BPM.

The BPM is represented by a one-dimensional model that consists of the region between and including the two reference electrodes in a four-probe electrochemical cell. By modeling this domain, all physical phenomena relevant to the measured polarization curves are captured: the Donnan equilibrium between the electrolytes and the ion-exchange layers, the transport of ionic species within the ion-exchange layers, and the electric-field-enhanced water dissociation occurring at the AEL/CEL junction. As shown in (Figure 2b), the model comprises a cathodic reference electrode (Ref 1), a 20 μm catholyte boundary layer (cBL), an 80 μm CEL, a 2.7 nm water-dissociation catalyst layer (CL), an 80 μm AEL, a 20 μm anolyte boundary layer (aBL), and an anodic reference electrode (Ref 2). The thickness of the ion-exchange layers is taken from manufacturer specifications (Fumatech) for the BPM used in the experiment.[4,39] The 2.7 nm thickness of the catalyst layer is a fitted parameter and is consistent with a previous study.[38] The thickness of the electrolyte boundary layers between the Luggin capillaries and the BPM were chosen for convenience, and the model results were insensitive to this choice (see Figure S1 in the Supporting Information). All of the parameters characterizing the membrane and the two electrolytes are listed in Table 1. This table also lists the diffusion coefficients for all species,

Table 1. List of Model Parameters and Their Source

parameter	value	unit	ref
membrane			
L_{AEL}	80	μm	39
L_{CEL}	80	μm	39
IEC	1.81	mmol g^{-1}	5
$\rho_{M.\ wet}$	1.0	g mL^{-1}	39
L_{char}	0.58	nm	23
electrolytes			
L_{aBL}	20	μm	assumed
L_{cBL}	20	μm	assumed
$c^0_{H_2O}$	55.56	mol L^{-1}	23
aqueous transport properties			
$D_{K^+,\,w}$	1.96×10^{-9}	m^2 s^{-1}	40
$D_{Na^+,\,w}$	1.33×10^{-9}	m^2 s^{-1}	40
$D_{SO_4^{2-},\,w}$	1.07×10^{-9}	m^2 s^{-1}	40
$D_{HSO_4^-,\,w}$	1.33×10^{-9}	m^2 s^{-1}	40
$D_{HPO_4^{2-},\,w}$	6.9×10^{-10}	m^2 s^{-1}	40
$D_{H_2PO_4^-,\,w}$	8.46×10^{-10}	m^2 s^{-1}	40
$D_{H_3O^+,\,w}$	6.96×10^{-9}	m^2 s^{-1}	23
$D_{OH^-,\,w}$	4.96×10^{-9}	m^2 s^{-1}	23
ε_{H_2O}	6.934×10^{-10}	F m^{-1}	23
ε_M	1.96×10^{-11}	F m^{-1}	23
homogeneous reactions			
K_1^0	3.26×10^{-18}		23
k_1^0	2.96×10^{-10}	m^3 (s mol)$^{-1}$	23
k_{-1}^0	9.08×10^{7}	m^3 (s mol)$^{-1}$	23
K_2	1.116×10^{-9}		41
k_{-2}	10×10^{11}	M^{-1} s^{-1}	42[a]
K_3	1.8×10^{-4}		41
k_{-3}	10×10^{11}	M^{-1} s^{-1}	42[a]

[a]Recombination rate constants were estimated from the work of Eigen,[42] which shows that acid recombination rate coefficients for various inorganic oxy-acids range from ~10^{10} M^{-1} s^{-1} to ~10^{11} M^{-1} s^{-1}. A value of 10^{11} M^{-1} s^{-1} for k_{-2} and k_{-3} was chosen for this study, and it is demonstrated that the polarization curves are relatively insensitive to these recombination rate constants as shown in Figures S3 and S4.

the dielectric coefficients of the membrane and water, and the rate and equilibrium constants for all reactions considered.

2.1. Kinetics of Water Splitting. To understand the electrochemical characteristics of BPMs, careful attention must be given to the dissociation of water to hydroxide and hydronium ions that can occur throughout the domain:

$$2H_2O \underset{k_{-1}}{\overset{k_1}{\rightleftharpoons}} H_3O^+ + OH^- \quad (1)$$

where k_1 and k_{-1} are the kinetic rate constants for water dissociation and recombination, respectively. For consistency with the kinetic parameters taken from Craig,[23] the bimolecular mechanism of water dissociation that involves the dissociation of two water molecules into hydroxide and hydronium is implemented as opposed to the pseudo-

https://dx.doi.org/10.1021/acsami.0c12686
ACS Appl. Mater. Interfaces 2020, 12, 52509−52526

unimolecular dissociation mechanism of one water molecule splitting to proton and hydroxide. The equilibrium constant for this homogeneous reaction is tabulated with the electrochemical potentials measured against a molar ratio reference state (see Section S2 of the Supporting Information for a derivation) as opposed to the standard reference state (again for consistency with Craig's work) and is therefore shifted by a factor of 55.56^2 from the standard reference value of 1×10^{-14}. This equilibrium constant is defined as

$$K_1^0 = \frac{k_1}{k_{-1}} = \frac{c_{OH^-} c_{H_3O^+}}{c_{H_2O}^2} \tag{2}$$

Prior studies have shown that the applied electric field at the junction of a BPM can achieve values up to 10^9 V m^{-1} attributed to the rapid change in background charge of the BPM at the AEL/CEL interface.[31,32] Under these very high fields, it is proposed that the rate of water dissociation is enhanced significantly, a phenomenon known as the Second Wien Effect, while the recombination rate changes only slightly, pushing the equilibrium toward dissociation.[23,43] To describe this phenomenon physically, first consider an undissociated water molecule as a dipole capable of dissociating. In order to dissociate, the dipole must first pass through a transition state for which the size of the dipole is equal to the Bjerrum length and dissociation becomes energetically favorable. Thermodynamically, when an electric field E is applied, the Gibbs free energy of the Bjerrum dipole transition state is reduced:[38,44]

$$\Delta G(E) - \Delta G(0) = -l_B e E, \quad l_B = \frac{e^2}{4\pi\epsilon k_B T} \tag{3}$$

where e is the elementary charge, l_B is the Bjerrum length, ϵ is the permittivity of free space, k_B is the Boltzmann constant, and T is the absolute temperature. This reduction in Gibbs free energy of the Bjerrum dipole transition state results in a corresponding increase in the escape rate of ions and thus the dissociation rate:[43]

$$\frac{k_1(E)}{k_1^0} = \exp\left(\frac{l_B e E}{k_B T}\right) = \exp\left(\frac{l_B F E}{RT}\right) \tag{4}$$

where k_1^0 is the dissociation rate coefficient in the absence of an applied electric field, F is the Faraday constant, and R is the ideal-gas constant. The value for k_1^0 is determined from the rate coefficients determined by Craig[23] evaluated at a temperature of 298 K. In prior studies,[31,32,45] this uncatalyzed electric-field dependence has been represented in the form

$$\frac{k_1(E)}{k_1^0} = \exp(\beta E) \tag{5}$$

where $\beta = \frac{l_B F}{RT}$ as per comparison with eq 6. We note that the form of eq 7 is consistent with the Butler–Volmer equation for describing the electrochemical kinetics of faradaic charge-transfer reactions at solid electrodes.[46,47] More complicated kinetic models have been proposed for the kinetics of water dissociation on various catalysts.[23,38] However, for simplicity in considering the impact of the catalyst, and due to the uncharacterized nature of water-dissociation catalysis for the Fumatech BPM, we choose to adopt an exponential behavior for the Second Wien Effect.

To incorporate the effect of the water-dissociation catalyst layer into the treatment of the Second Wien Effect, a similarity in behavior to Butler–Volmer kinetics is invoked and a parameter α, which will be referred to as the catalyst effectiveness factor, is introduced, which is treated like the charge-transfer coefficient in the Butler–Volmer equation:

$$\frac{k_1(E)}{k_1^0} = \exp(\alpha\beta E) \tag{6}$$

where α is defined to be 1 in all regions outside of the water-dissociation catalyst layer, preserving the proposed kinetics of the non-catalytically assisted water dissociation (eq 7). On the other hand, in the 2.7 nm thick catalyst layer, the value of α is fit to a value of 1.8. Because there is no explicit treatment of both an uncatalyzed and a catalyzed pathway within the catalyst layer, this effectiveness factor should be thought of as describing a composite of both pathways.

Recombination is also impacted by the presence of an applied electric field, albeit to a much lesser extent. By following the methodology of Onsager and Fuoss,[48] one can derive the following formulation for the recombination rate constant:[23]

$$\frac{k_{-1}(E)}{k_{-1}^0} = 1 + \frac{1 - \exp\left(-\frac{1}{\sigma}\right)}{2}\left(\sigma^2\beta E + (4.97\sigma)\frac{\sinh(0.0835\sigma\beta E)}{\cosh^2(0.0835\sigma\beta E)}\right), \quad \sigma = \frac{a}{2l_B} \tag{7}$$

The parameter σ represents a dimensionless bond length for recombination and is based on the physical bond length for water dissociation and recombination where a = 0.58 nm.[23]

2.2. Homogeneous Buffer Reactions. In addition to the dissociation of bulk water within the BPM, the homogeneous buffer reactions of the co- and counter-ions are considered. Doing so contributes to a complete electrochemical description of the BPM, which is critical at low current densities where co- and counter-ion transport dominates. For the electrolytes studied (i.e., sulfate and phosphate), these buffer reactions, which occur in both the aqueous and ionomer phases, are given by

$$H_2PO_4^- + H_2O \underset{k_{-2}}{\overset{k_2}{\rightleftharpoons}} H_3O^+ + HPO_4^{2-} \tag{8}$$

$$HSO_4^- + H_2O \underset{k_{-3}}{\overset{k_3}{\rightleftharpoons}} H_3O^+ + SO_4^{2-} \tag{9}$$

Both buffer reactions are considered in their bimolecular form for consistency with the bimolecular water-dissociation mechanism employed in the present study (see eq 3). The equilibrium constants, K_i, for eqs 10 and 11 are taken from the literature[41] and converted to the molar ratio reference (see derivation in Section S2 of the Supporting Information), which shifts their values by a factor of 55.56 compared to the standard reference (see values given in Table 1). In this model, the first buffer dissociation is assumed to be complete and the molecular forms of sulfuric acid or phosphoric acid are assumed to be absent. Additionally, while hydrogen phosphate (HPO_4^{2-}) can further dissociate to phosphate (PO_4^{3-}) anions, because the K_a for hydrogen phosphate is very small ($K_a = 4.2 \times 10^{-13}$), this dissociation is neglected.

The forward rate coefficients for all dissociation reactions are taken to be large enough to ensure equilibrium of the buffered species throughout the domain over the range of applied membrane potential (0–1 V). The rate coefficients for the reverse reactions are given by

$$K_n = \frac{k_n}{k_{-n}} \tag{10}$$

The work by Divekar *et al.* suggests that the rate coefficients and the unimolecular K_a of the buffer reactions change when measured in an ionomer environment as opposed to an aqueous solution.[49] Because the magnitudes of these differences have not yet been established and likely vary with membrane hydration, co- and counter-ion identity, etc., they are neglected in this study; the magnitude of the rate coefficients and equilibrium constants are treated as the same in both the membrane and the electrolyte.[50−52]

2.3. Treatment of Membrane Fixed Charge. The fixed-charge density between the different regions in the membrane is modeled using hyperbolic tangents:[23]

$$c_M(x) = \frac{\rho_{M,wet} \times IEC}{2}\left(\tanh\left(\frac{x - x_3}{L_{char}}\right) - \tanh\left(\frac{x - x_4}{L_{char}}\right) + \tanh\left(\frac{x - x_2}{L_{char}}\right) - \tanh\left(\frac{x - x_1}{L_{char}}\right)\right) \tag{11}$$

https://dx.doi.org/10.1021/acsami.0c12686
ACS Appl. Mater. Interfaces 2020, 12, 52509−52526

Here, x is the position as measured from the center of the BPM. x_1 is the leftmost point of the CEL, x_2 is the leftmost point of the catalyst layer, x_3 is the leftmost point of the AEL, and x_4 is the leftmost point of the anolyte boundary layer (see Figure 2). This distribution is illustrated in Figure S5. Equation 13 allows for smooth, differentiable transitions (i.e., a smoothed step function) at the interface between the electrolyte and ionomer phases as well as between the AEL and CEL. The hyperbolic tangents in this study have a characteristic length of L_{char} = 0.58 nm, which is the characteristic bond length for water dissociation derived by Craig, and represents the length at which the hydroxide and hydronium ions separate and start to diffuse apart from one another.[23]

2.4. Electrochemical Potentials. To construct a thermodynamically consistent model, expressions for the electrochemical potential of the various ionic species are required.[47] For the BPM, these electrochemical potentials are dependent on temperature, pressure, composition, electrostatic potential, and applied electric field.[23] For the present study, the system is assumed isothermal at 298 K and isobaric at 1 bar pressure. The electrochemical potentials employed (see Table 2) are also defined based on the molar ratio of the ionic species concentration to the local water concentration.[23] Due to the choice of this molar ratio reference state (see Section S2), the local water concentration appears in the definition for the electrochemical potential of a given ionic species. This allows the model to capture the effects of water concentration gradients that develop within the BPM on the electrochemical potential and thus transport of each ionic species. Because the electrochemical potential is solved for all aqueous and ionomer phases and for all ionic species, Donnan equilibrium with the bulk electrolyte is implicitly obeyed in terms of the partitioning of the ionic species between the ionomer phase and the bulk electrolyte (see Section S4 in the Supporting Information for Donnan equilibrium calculation).[53]

Table 2. Chemical and Electrochemical Potentials of Species Present in the Model[a]

species	potential
H_3O^+	$\tilde{\mu}_{H_3O^+} = \tilde{\mu}^0_{H_3O^+} + RT\ln\left(\frac{c_{H_3O^+}c^0_{H_2O}}{c^0_{H_3O^+}c_{H_2O}}\right) + F\Phi + RT\ln(\gamma^E_\pm)$
OH^-	$\tilde{\mu}_{OH^-} = \tilde{\mu}^0_{OH^-} + RT\ln\left(\frac{c_{OH^-}c^0_{H_2O}}{c^0_{OH^-}c_{H_2O}}\right) - F\Phi + RT\ln(\gamma^E_\pm)$
co- and counter-ions	$\tilde{\mu}_i = \tilde{\mu}^0_i + RT\ln\left(\frac{c_i c^0_{H_2O}}{c^0_i c_{H_2O}}\right) + z_i F\Phi$

[a] $\mu^0_{H_2O}$ is the chemical potential of pure water at 1 bar. For any ionic species, $\tilde{\mu}^0_i$ is a reference state for species i in water at 1 bar, c_i is the concentration of species i, c^0_i is the concentration of the species i at the reference conditions, z_i is the charge of the ion, and Φ is the macroscopic electrostatic potential.

For the special case of hydronium and hydroxide, an electric-field-dependent activity coefficient, $\gamma^E_\pm$, is needed to maintain thermodynamic consistency due to the electric-field dependence of the dissociation equilibrium resulting from the Second Wien Effect. This field-dependent activity coefficient is determined by solving for the activity coefficient necessary to satisfy equilibrium between the hydronium, hydroxide, and water ($\tilde{\mu}_{H_3O^+} + \tilde{\mu}_{OH^-} = 2\tilde{\mu}_{H_2O}$) throughout the domain:

$$\gamma^E_\pm = \sqrt{\frac{k_1{}^0 k_{-1}(E)}{k_{-1}{}^0 k_1(E)}} \tag{15}$$

2.5. Transport Equations. The fluxes of the mobile ions are governed by the generalized Nernst–Planck equation:

$$N_i = -\frac{D_i c_i}{RT}\frac{d\tilde{\mu}_i}{dx} \tag{16}$$

where N_i is the molar flux of species i, and D_i is the diffusivity of species i. The Nernst–Einstein relationship is used to relate mobilities and diffusivities. Substitution of eqs 14–16 into eq 18 yields the flux of each individual ionic species, as shown in Table 3.

Typically, Stefan–Maxwell diffusion is used to capture species/species interactions that are significant in concentrated systems. Unfortunately, because our model describes the transport of up to seven ionic species, implementation of the Stefan–Maxwell framework would require an additional 42 degrees of freedom as well as the determination of composition-dependent diffusion coefficients for the frictional interactions between the seven salt-ion species, water, and the membrane. This would increase the uncertainty and complexity of the numerical model considerably; consequently, the Nernst–Planck equation is used even though the conditions are not necessarily dilute. We also note that, in the present study, we only simulate current densities up to 10 mA cm^{-2}, for which the dilute-solution theory has been found to be sufficiently accurate.[54]

The diffusion coefficients for a given ionic species, D_i, depend on the phase. In the aqueous electrolyte phases, these diffusion coefficients are equal to their values in pure water, $D_{i,w}$. In the ionomer phase, the effective diffusion coefficients for each ionic species, $D_{i,eff}$ are calculated following work of Grew *et al.*:[53,55,56]

$$D_{i,eff} = \frac{\phi_L^q D_{i,w}}{x_w\left(1 + \frac{1}{\lambda}\zeta_i\right)} \tag{20}$$

In this framework, q is a fitting parameter related to the tortuosity of the ionomer and x_w is the ratio of the moles of water in the membrane to the sum of the moles of water and fixed-charge groups given by

Table 3. Flux of Ionic Species in the Model

species	flux
H_3O^+	$N_{H_3O^+} = -D_{H_3O^+}\frac{dc_{H_3O^+}}{dx} + D_{H_3O^+}c_{H_3O^+}\frac{d(\ln(c_{H_2O}))}{dx} + D_{H_3O^+}c_{H_3O^+}\frac{FE}{RT} - D_{H_3O^+}c_{H_3O^+}\frac{d(\ln(\gamma^E_\pm))}{dx}$
OH^-	$N_{OH^-} = -D_{OH^-}\frac{dc_{OH^-}}{dx} + D_{OH^-}c_{OH^-}\frac{d(\ln(c_{H_2O}))}{dx} - D_{OH^-}c_{OH^-}\frac{FE}{RT} - D_{OH^-}c_{OH^-}\frac{d(\ln(\gamma^E_\pm))}{dx}$
co- and counter-ions	$N_i = -D_i\frac{dc_i}{dx} + D_i c_i\frac{d(\ln(c_{H_2O}))}{dx} + z_i D_i c_i\frac{FE}{RT}$

https://dx.doi.org/10.1021/acsami.0c12686
ACS Appl. Mater. Interfaces 2020, 12, 52509–52526

$$x_w = \frac{\lambda}{1+\lambda} \tag{21}$$

where λ is the hydration of the ion-exchange layer defined as the ratio of water molecules in the ionomer to fixed-charge groups. ϕ_L is the water volume fraction in the ionomer:

$$\phi_L = \frac{\lambda V_w}{\lambda V_w + V_M} \tag{22}$$

where V_w and V_M are the molar volumes of pure water and membrane, respectively. The parameter ζ_i describes the ratio of the species-water and species-membrane diffusivities and can be approximated by the kinetic theory:[57]

$$\zeta_i = \frac{D_{i,w}}{D_{i,M}} = \left(\frac{V_M}{V_w}\right)^{2/3}\left(\frac{M_{i,M}}{M_{i,w}}\right)^{1/2} \tag{23}$$

where $M_{i,M} = \left(\frac{1}{M_i} + \frac{1}{M_M}\right)$ is the reduced molar mass.

From these fluxes, material balances for each species provide governing equations for the steady-state model:

$$\frac{dN_i}{dx} = R_i \tag{24}$$

where R_i is the production of species i from homogeneous chemical reactions:

$$R_i = \sum_n s_{i,n}\left(k_n \prod_{s_{i,n}<0} c_i^{-s_{i,n}} - k_{-n}\prod_{s_{i,n}>0} c_i^{s_{i,n}}\right) \tag{25}$$

where $s_{i,n}$ is the stoichiometric coefficient of species i in reaction n.

To solve for the potential, Poisson's equation is employed:

$$-\frac{d^2\Phi}{dx^2} = \frac{F}{\varepsilon}\left(c_M(x) + \sum_i z_i c_i\right) \tag{26}$$

where ε is the permittivity of the medium and is expected to vary from the aqueous solution to the membrane. The permittivity of the BPM is expected to be similar to that of a dioxane−water mixture and is given as a function of the local water content by Craig:[23,58,59]

$$\varepsilon = \left(\frac{c^M_{H_2O}}{c^0_{H_2O}}\varepsilon^{-1}_{H_2O} + \varepsilon_M^{-1}\left(1 - \frac{c^M_{H_2O}}{c^0_{H_2O}}\right) + \varepsilon_3^{-1}\right)^{-1} \tag{27}$$

where ε_M is the permittivity of pure dioxane, ε_{H_2O} is the permittivity of pure water, and ε_3 is a mixing term that takes into account interactions between the ionomer and absorbed water:

$$\varepsilon_3 = \varepsilon_0\left(\frac{-2.42\left(1 - \frac{c^M_{H_2O}}{c^0_{H_2O}}\right)\frac{c^M_{H_2O}}{c^0_{H_2O}}}{-0.48\left(1 - \frac{c^M_{H_2O}}{c^0_{H_2O}}\right) - 5.03\frac{c^M_{H_2O}}{c^0_{H_2O}}} + 0.066\left(1 - \frac{c^M_{H_2O}}{c^0_{H_2O}}\right)\frac{c^M_{H_2O}}{c^0_{H_2O}}\right)^{-1} \tag{28}$$

This mixing term is quite significant and can account for up to a 40% difference in permittivity for a BPM fully exchanged with hydronium or hydroxide.

Lastly, the electric field and electrostatic potential are related by

$$\frac{d\Phi}{dx} \equiv -E \tag{29}$$

2.6. BPM Water Uptake. It has been shown that the water uptake in BPMs is significantly lower from that in Nafion or other well-characterized ionomers (λ = 9 for a BPM vs λ = 21 for Nafion).[5,60,61] There is a lack of available data regarding the transport coefficients or water-uptake isotherms for BPMs, and measured properties of monopolar membranes are not a sufficient proxy for modeling BPM water transport. Therefore, rather than solving for the water chemical potential and water flux explicitly, which are nontrivial and quite complicated, the concentration of water in the BPM is assumed to follow a complementary functional form to that for the fixed charge (eq 13). Therefore, the water concentration is given by

$$c_{H_2O}(x) = \frac{c^0_{H_2O}}{2}\left(2 - \tanh\left(\frac{x-x_1}{L_{char}}\right) + \tanh\left(\frac{x-x_4}{L_{char}}\right)\right) + \frac{c^M_{H_2O}}{2}\left(\tanh\left(\frac{x-x_1}{L_{char}}\right) - \tanh\left(\frac{x-x_4}{L_{char}}\right)\right) \tag{30}$$

where $c^0_{H_2O}$ is the concentration of pure aqueous phase water (55.56 M), and $c^M_{H_2O}$ is the concentration of water in the ionomer phase:

$$c^M_{H_2O} = \lambda(\rho_{M,wet} \times IEC) \tag{31}$$

where $\rho_{M,wet}$ is the density of the hydrated membrane and IEC is the ion-exchange capacity of the BPM. These parameters are assumed to be the same for both layers.

The water content, λ, defined as the molar ratio of water to fixed ion-exchange groups in the CEL and AEL, are dependent on the internal hydronium or hydroxide content (see Figure S6):[21]

$$\lambda_{CEL} = \lambda_{f_{H_3O^+}=0} + f_{H_3O^+}\lambda_{f_{H_3O^+}=1} \tag{32}$$

$$\lambda_{AEL} = \lambda_{f_{OH^-}=0} + f_{OH^-}\lambda_{f_{OH^-}=1} \tag{33}$$

where $\lambda_{f_{H_3O^+}=0}$ and $\lambda_{f_{OH^-}=0}$ are the hydration of a completely salt-ion-exchanged CEL and AEL, respectively, $\lambda_{f_{H_3O^+}=1}$ is the hydration of the proton-form CEL, and $\lambda_{f_{OH^-}=1}$ is the hydration of the hydroxide-form AEL. $f_{H_3O^+}$ is the fraction of hydronium ions calculated at every point in the CEL:

$$f_{H_3O^+} = \frac{c_{H_3O^+}}{IEC \times \rho_{M,wet}} \tag{34}$$

f_{OH^-} is the fraction of hydroxide ions calculated at every point in the AEL:

$$f_{OH^-} = \frac{c_{OH^-}}{IEC \times \rho_{M,wet}} \tag{35}$$

$\lambda_{f_{H_3O^+}=0}$ and $\lambda_{f_{OH^-}=0}$ are both fit to a value of 6 in order to ensure consistency between the salt-ion current in the measured and simulated polarization curves and are consistent with the lower uptake of salt forms of the membranes.[20,21,60] $\lambda_{f_{H_3O^+}=1}$ and $\lambda_{f_{OH^-}=0}$ are both taken from measurements of BPM water uptake in DI water (λ = 9).[5]

As noted in the previous subsections, explicit water species/membrane interactions are not included in the model. However, such interactions are included implicitly in the treatment of water uptake, diffusivity, and dielectric permittivity. These interactions will be important to model but are beyond the scope of the current study, largely because these interactions in BPMs have not yet been characterized fully and will likely differ substantially from those measured in monopolar membranes. Further experimental work is necessary to characterize BPM transport properties so that they can be implemented in future transport studies.

2.7. Boundary Conditions. The boundary conditions for the model are comprised of Dirichlet boundary conditions at each reference electrode. The potential of Ref 1 is held at 0.0 V, and the potential of Ref 2 is set to the applied membrane potential as measured experimentally. The concentration of the ionic species at Ref 1 (the catholyte boundary) is the concentration of the ionic species present in the bulk catholyte. Similarly, the concentration of the ionic species at Ref 2 (the anolyte boundary) is the concentration of ionic species in the bulk anolyte. Four pH environments are considered that are relevant to efficient electrolysis and electrosyn-

https://dx.doi.org/10.1021/acsami.0c12686
ACS Appl. Mater. Interfaces 2020, 12, 52509−52526

thesis, as previously discussed, and correspond to those of Vermaas *et al.*:[4] a neutral pH 7-7 environment with both catholyte and anolyte as a mixture of 0.45 M K_2HPO_4 and 0.55 M KH_2PO_4 (this will be referred to as 1 M $K_iH_jPO_4$ where $i + j = 3$ or simply KP_i); a pH 0-7 environment with a 1 M H_2SO_4 catholyte and a 1 M $K_iH_jPO_4$ anolyte, a pH 7-14 environment with a 1 M $K_iH_jPO_4$ catholyte and a 1 M KOH anolyte, and a 0−14 pH environment with a 1 M H_2SO_4 catholyte and a 1 M KOH anolyte. In addition to the electrolyte pairs considered by Vermaas *et al.*,[4] polarization curves were collected experimentally (see Section S6 in the Supporting Information for experimental protocol) and modeled for a pH 0-7 environment with a 1 M HCl catholyte and either a 1 M Na_2SO_4 or 1 M $K_iH_jPO_4$ anolyte.

2.8. Numerical Methods. The governing equations (ionic species material balances and Poisson equation) were modeled in the General Form PDE Module and were solved with the MUMPS general solver in COMSOL Multiphysics 5.5 with a relative tolerance of 0.001 (see equations presented in Section S7). The modeling domain was discretized with a nonuniform mesh comprised of 1084 elements, which used an exponential refinement near the electrolyte/ionomer and AEL/CEL interfaces in order to capture the sharp concentration gradients of about 0.58 nm characteristic length. A mesh independence study was performed (see Figure S2 in the Supporting Information) revealing that a mesh of at least 412 domain elements is required to achieve convergence. For meshes finer than 412 elements, the model is completely independent of the chosen domain meshing.

3. RESULTS AND DISCUSSION

3.1. Polarization Curves for Various Electrolytes. Simulations were conducted for the four electrolyte environments investigated experimentally by Vermaas *et al.*[4] For each of the four environments, the model was fit to the measure polarization curve by adjusting the fitting parameters listed in Table S3. These fitting parameters are the same for all four pH environments. As seen in Figure 3, the model exhibits the characteristics of typical BPM polarization curves. There is an initial regime between 0.0 and ∼0.6 V that is strongly mass-transfer limited and corresponds to the crossover of electrolyte salt ions. Beyond ∼0.6 V, the electric field at the junction becomes sufficient to shift the equilibrium toward water dissociation through the Second Wien Effect, and the BPM enters a water-dissociation-controlled regime, where the current is primarily dictated by the production of hydronium and hydroxide ions at the interface.[19,23] These distinct regimes are well represented in the polarization curves for pH 7-7, pH 0-7, and pH 7-14. The pH 0-14 case does not exhibit a salt-ion transport regime because the large dissociation and recombination currents present in this pH environment obscure the co- and counter-ion crossover. In contrast to earlier models, which have had difficulty capturing electrochemical characteristics of the BPM in the salt-ion-leakage regime, the agreement between the model and experimental results is quite strong throughout the entire window of applied potentials. This model is also one of the first to capture the effects of an applied pH gradient. This is an important advance because it provides critical insights needed for the implementation of BPMs in electrolyzers with optimal environments for electrosynthesis.[4,5,14]

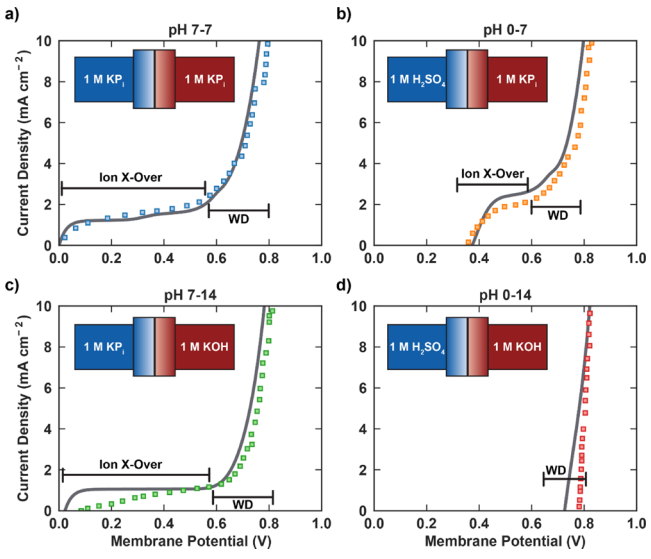

Figure 3. Calculated (solid lines) and measured (markers) polarization curves describing electrochemical behavior of bipolar membranes across various pH gradients. Experimental curves adapted from the data in reference 4: (a) pH 7-7, (b) pH 0-7, (c) pH 7-14, and (d) pH 0-14. Brackets depict the regimes (salt-ion crossover and water dissociation) present in each polarization curve. Regimes are defined by the phenomenon dominating transport in each applied voltage window. Inset schematic displays the corresponding electrolyte combination for each modeled polarization curve.

Although the simulated polarization curves agree very well with those observed experimentally within the water dissociation regime for all pH ranges explored, there is some disagreement between the simulated and experimental polarization curves for the salt-ion crossover regime for pH 7-7 and pH 7-14. Specifically, while the mass-transfer limit (∼1 mA cm^{-2}) is identical for both the modeled and experimental polarization curves for pH 7-14, the experimental curve attains its mass-transfer limit at a much higher membrane potential, whereas the simulated polarization curve has a much sharper and earlier transition to the mass-transfer limited regime. Additionally, while the simulated curve for pH 7-7 exhibits two distinct plateaus in current density, the experimental data from Vermaas does not. These discrepancies can be initially rationalized by recognizing that the simulations presented here assume a steady state, whereas the experiments reported by Vermaas *et al.* were carried out using a galvanostatic sweep of 0.03 mA cm^{-2} s^{-1}.[4] Because of the transient nature of the galvanostatic sweep, it is possible that, during the experiments, the BPM did not have ample time to achieve equilibrium in the salt-ion regime, and consequently a slower approach to its mass-transfer limitations for pH 7-14 was observed. This slower approach to equilibrium also obscures the distinct plateaus for the 7-7 case. Nonetheless, we find that the steady-state model adequately captures the essential physics of the BPM in these environments; modeling a transient BPM is beyond the scope of the current work.

3.2. Analysis of Partial Current Densities in a BPM. In addition to describing the polarization curve for a BPM, the model can be used to decompose the current density into the partial-current-density contributions for each ionic species. The ability to do so is important because there is still disagreement between experimentalists regarding the primary carrier of current in each regime of the polarization curve. Most investigators have argued that in the mass-transfer-limited regime, referred to above as the salt-ion crossover regime, the current is solely due to the transport of electrolyte salt ions.[19,33] However, by fully modeling and deconvoluting the contributions of individual ions to current density in the pH environments explored, the present model demonstrates that, while the plateau current density is largely dominated by the transport of salt ions, hydronium and hydroxide ion

https://dx.doi.org/10.1021/acsami.0c12686
ACS Appl. Mater. Interfaces 2020, 12, 52509−52526

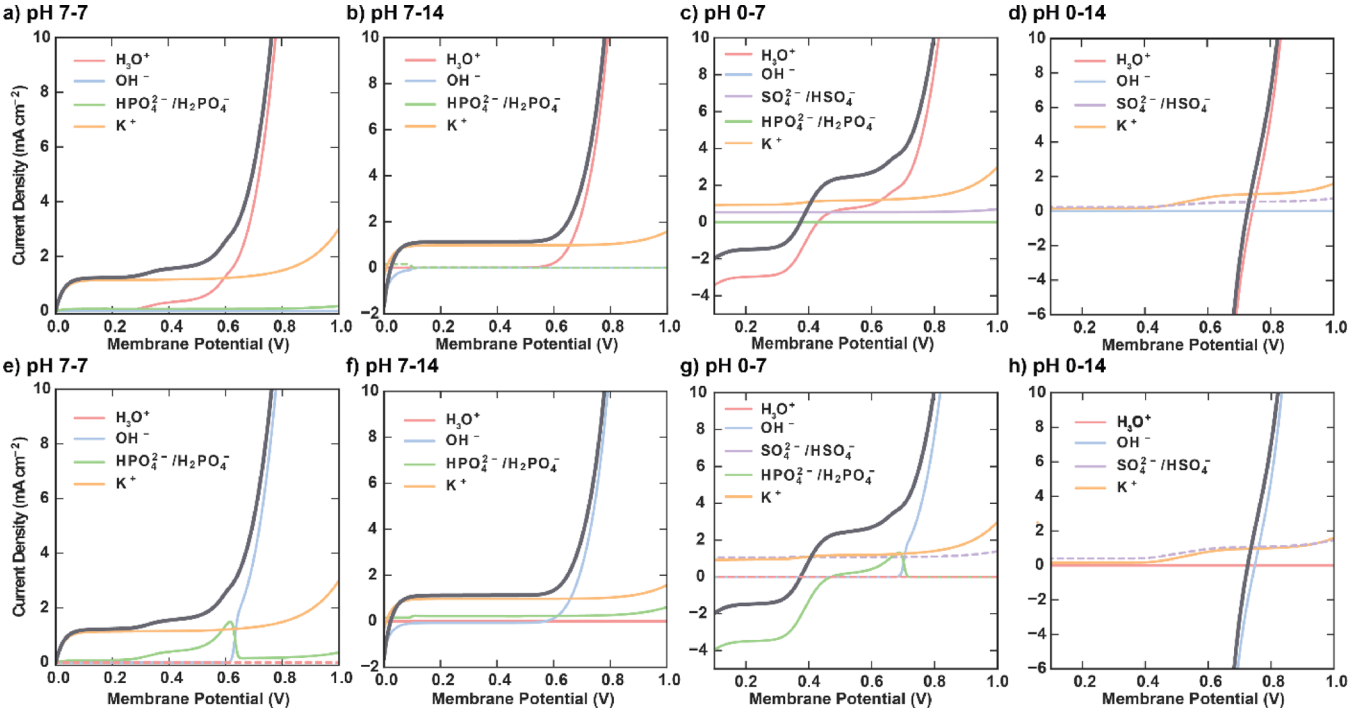

Figure 4. Analysis of partial current densities in the BPM. (a–d) Polarization curve breakdown into partial current density contributions for species in the CEL. (e–h) Polarization curve breakdown into partial current density contributions for species in the AEL. Dashed lines are purely for visibility of overlapping curves.

currents generated by water dissociation account for a significant portion of the overall current density.

Figure 4 displays the polarization curves (gray curves) decomposed into their contributions (colored curves) for each ionic species for the four pH environments modeled. Due to differing sign of the background charges in each ionomer layer, there are stark differences in the ionic currents in each layer. The current in the CEL is primarily carried by cations, and the current in the AEL is carried by anions. Therefore, the partial current densities for the CEL (Figure 4a–d) and AEL (Figure 4e–h) are distinct from one another. In examining these partial-current distributions, the argument for a distinct salt-ion crossover regime and a distinct water-dissociation regime becomes clear. As shown in Figure 4a–d, at low current densities, the current density in the CEL is dominated initially by potassium transport (orange curves). However, once significant water dissociation occurs (referred to as breakdown) and hydronium cations are generated in the CEL, the shape of the polarization curve becomes dictated by the hydronium partial current density (red curves). This conclusion is further demonstrated in the partial current distributions in the AEL (Figure 4e–h). For low current densities, potassium and phosphate-species (green curves) crossover dominate the electrochemical behavior. However, when breakdown is achieved at high current densities, a sharp transition is visible into a regime where hydroxide ions formed at the interface account for most of the current carried in the AEL. This demonstrates that the plateau observed in the polarization curve is indeed due to mass-transfer-limited co- and counter-ion crossover.

These two distinct regimes are not observed for the case of pH 0-14. As shown in Figure 4d,h, the potassium (orange) and sulfate (purple) currents achieve a value of up to ∼1.5 mA cm^{-2} for a membrane potential of 1 V, which is comparable to the co- and counter-ion current achieved in other pH environments. Hence, the salt-ion contributions thus account for a significant portion of the overall current. However, the salt-ion contribution is almost totally obscured due to the steep slopes of the hydronium and hydroxide currents carried in the CEL and AEL, respectively.

To address the distribution of ionic current densities in the plateau current density, the fractions of the total current carried by hydronium and hydroxide ions were calculated (partial current divided by total current) and plotted against total current density (Figures S9 and S10 in the Supporting Information). As seen in Figure 4, the plateau in current densities for the polarization curves occurs at ∼1 to 2 mA cm^{-2}. Calculation of the fraction of the current due to water dissociation at these current densities reveals that water dissociation is responsible for up to 40% of the current in the plateau. This demonstrates that, while co- and counter-ion crossover does indeed dominates at low current densities and applied potentials, interfacial water dissociation is responsible for a non-negligible portion of the measured current.

3.3. Hydronium and Hydroxide Concentration Polarization and Transport Mechanisms. Concentration gradients in hydronium and hydroxide ions are particularly relevant when considering a BPM device, where the gradients affect membrane water uptake and drive ionic transport.[21,61] Vermaas *et al.* hypothesized that hydronium and hydroxide concentration polarization would occur within the BPM due to the generation of ions from water dissociation at the CEL/AEL interface.[4] Additionally, Sun *et al.* hypothesized that the concentration polarization would be greater within the AEL than in the CEL due to the lower diffusivity of hydroxide in comparison to hydronium.[18] Both of these effects are captured well by the model for ion-exchange layers in contact with a neutral electrolyte (Figure 5a). At potentials larger than the

https://dx.doi.org/10.1021/acsami.0c12686
ACS Appl. Mater. Interfaces 2020, 12, 52509–52526

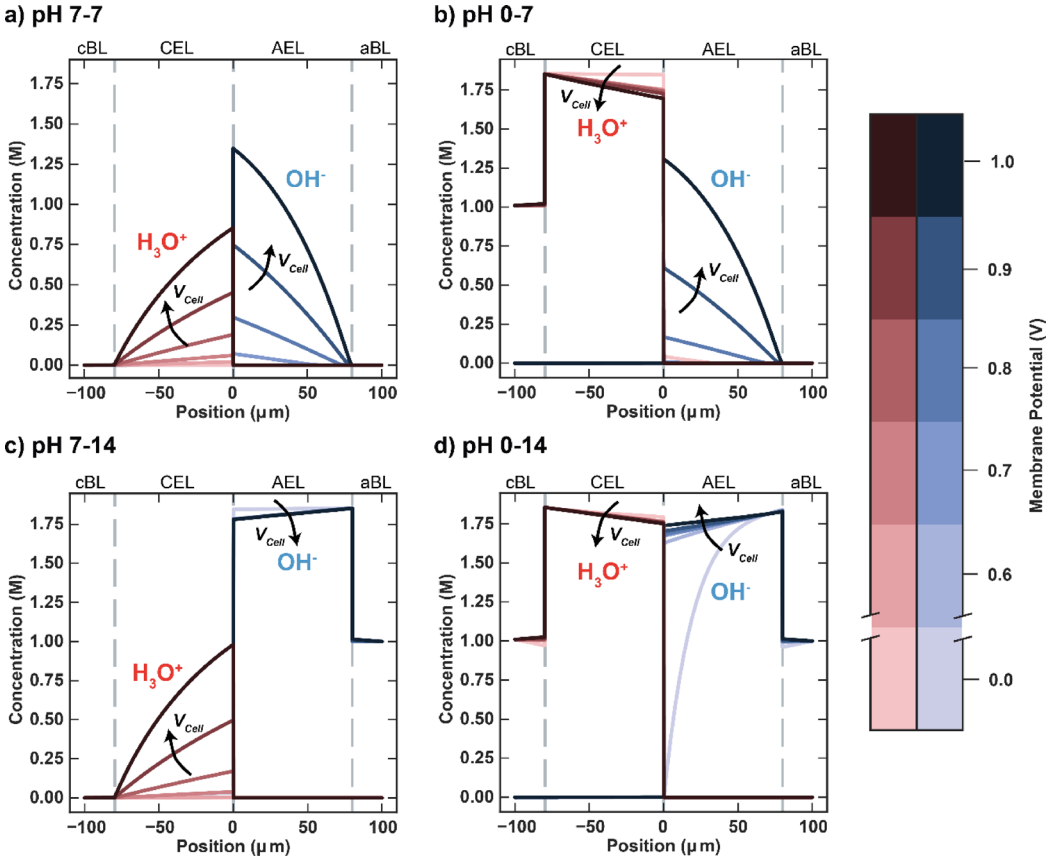

Figure 5. Hydronium and hydroxide concentration profiles at various applied potentials for four modeled pH environments: (a) pH 7-7, (b) pH 0-7, (c) pH 7-14, and (d) pH 0-14. Arrows represent the direction of increasing membrane potentials.

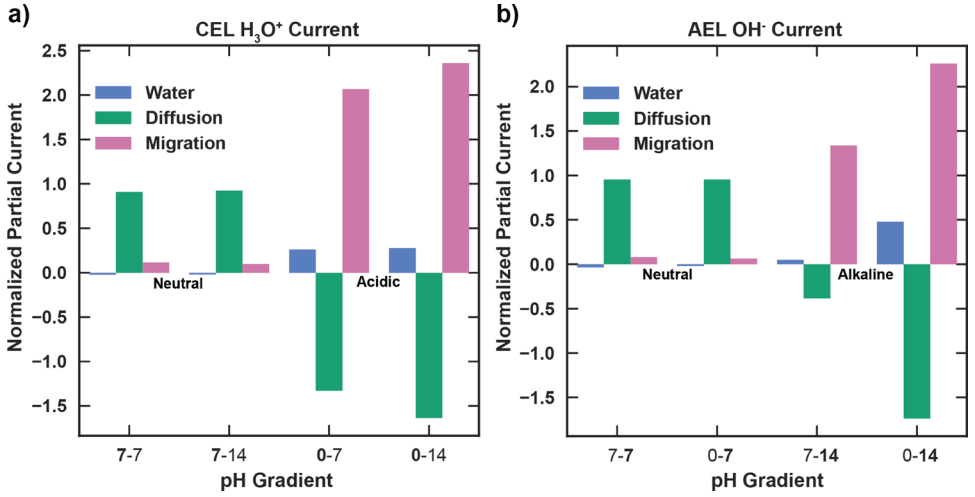

Figure 6. Breakdown of mechanistic contributions to (a) hydronium current in the CEL and (b) hydroxide current in the AEL at an applied potential of 0.8 V. All mechanistic partial currents are normalized by the total hydronium current or hydroxide current, respectively. Labels under bars display the neutrality, acidity, or alkalinity of the electrolyte adjacent to the given ion-exchange layer. Normalized mechanistic contributions are calculated as an average of the value in the given ion-exchange layer.

breakdown potential, strong concentration gradients in the simulated hydronium and hydroxide profiles form to preserve electroneutrality with the salt ions within the BPM. These concentration gradients are generated as follows. At the AEL/CEL interface, both hydronium and hydroxide species achieve maximum concentrations due to water dissociation. Conversely, at the ionomer/electrolyte interfaces, the hydronium and hydroxide concentrations are significantly lower consistent with the Donnan equilibrium between the ionomer and the neutral electrolyte phases. Moreover, the simulated hydroxide concentration gradients at a given voltage are larger than the corresponding hydronium gradients. As the applied voltage increases, the degree of concentration polarization observed also increases, which corresponds to an increase in ion transport by diffusion.

https://dx.doi.org/10.1021/acsami.0c12686
ACS Appl. Mater. Interfaces 2020, 12, 52509−52526

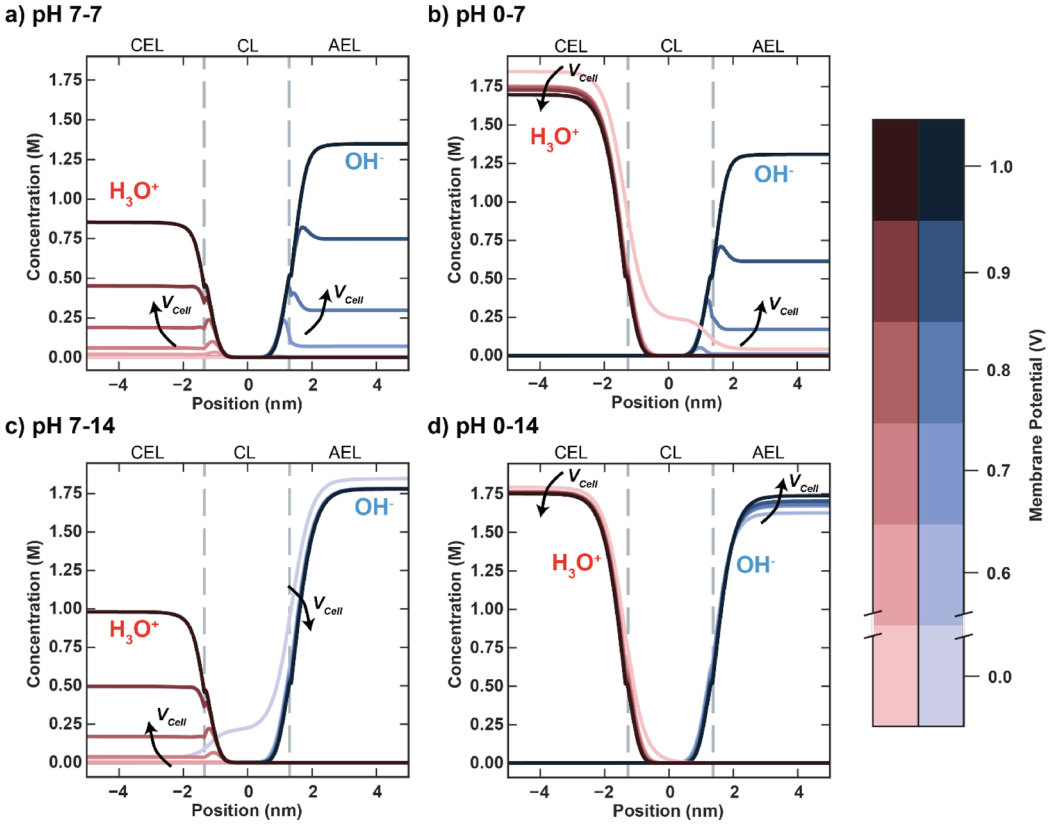

Figure 7. Hydronium and hydroxide concentration profiles in the depletion region at the AEL−CEL interface for various applied voltages in four modeled pH environments: (a) pH 7-7, (b) pH 0-7, (c) pH 7-14, and (d) pH 0-14 (zoomed-in plot of Figure 5). Arrows represent the direction of increasing membrane potential.

Concentration polarization is not apparent for a CEL in contact with a highly acidic (pH 0) or an AEL in contact with a highly alkaline (pH 14) electrolyte. For these cases, because the hydronium or hydroxide ions are the majority carriers in the electrolyte solution, the corresponding ion-exchange layer is already fully exchanged with hydronium or hydroxide once Donnan equilibrium is achieved. The dissociation of water at the interface is therefore incapable of imposing concentration gradients in the hydronium and hydroxide ions the membrane, and the gradients in electrostatic potential (Figure S11 in the Supporting Information) must be the driving force for the migration of hydronium and hydroxide. Prior work in BPMs has consistently reinforced the concept that all gradients in electrostatic potential outside of the bipolar junction are negligible.[18,31,32] While these electrostatic potential gradients in the bulk ionomer are small (as depicted in Figure S11), the current study finds that, for an ion-exchange layer in contact with a strong acid or base, migration is indeed the dominant mode of transport for hydronium or hydroxide ions.

As demonstrated, the concentration profiles for hydronium and hydroxide are particularly pertinent to understanding multi-ion transport in a BPM because, when coupled with the electrostatic potential profiles, they elucidate the driving force for transport within each ion-exchange layer for a given electrolyte pairing. Figure 6 depicts the relative contributions of diffusive transport $(-D_i\frac{dc_i}{dx})$ and migration $(z_iD_ic_i\frac{FE}{RT})$, in addition to contributions to transport due to water concentration gradients $(D_ic_i\frac{d(\ln(c_{H_2O}))}{dx})$, for the four applied pH gradients at a membrane potential of 0.8 V. In all cases, the fluxes of hydronium and hydroxide ions due to water concentration gradients within the BPM are small but contribute in a non-negligible manner to the measured ionic current. Nonetheless, for ion-exchange layers in contact with a neutral electrolyte, the majority (~90%) of the hydronium or hydroxide current density is carried by diffusion. This is expected due to the large concentration gradients that result from interfacial water dissociation. Conversely, for ion-exchange layers in contact with an acidic or alkaline electrolyte, the hydronium or hydroxide current is dominated by migration. In fact, for these cases, the driving force for diffusion opposes the reverse bias and must be overcome by the electrostatic potential driving force for migration. These conclusions demonstrate that there is a distinct change in the mechanism of transport for a BPM in a harsh applied pH gradient compared to what occurs for a BPM submersed in a neutral salt. This mechanistic change in BPM transport for very high or low pHs is vital toward understanding BPMs for electrolysis or electrosynthesis applications.

Keys to the electrochemical characteristics of a BPM are the hydronium and hydroxide profiles at the interface between the AEL and the CEL. It is in this region that the electric field (Figure S12 in the Supporting Information) achieves its maximum and electroneutrality is broken (see Figure 7), thereby enabling the dissociation of water.[23,31,32] Mafé *et al.* predicted the formation of a "depletion zone" locally surrounding the AEL/CEL interface where there is an absence of mobile hydronium or hydroxide charges.[31] The analytical solution by Mafé also predicts that the double-layer thickness would be a function of membrane potential and be between 2

https://dx.doi.org/10.1021/acsami.0c12686
ACS Appl. Mater. Interfaces 2020, 12, 52509−52526

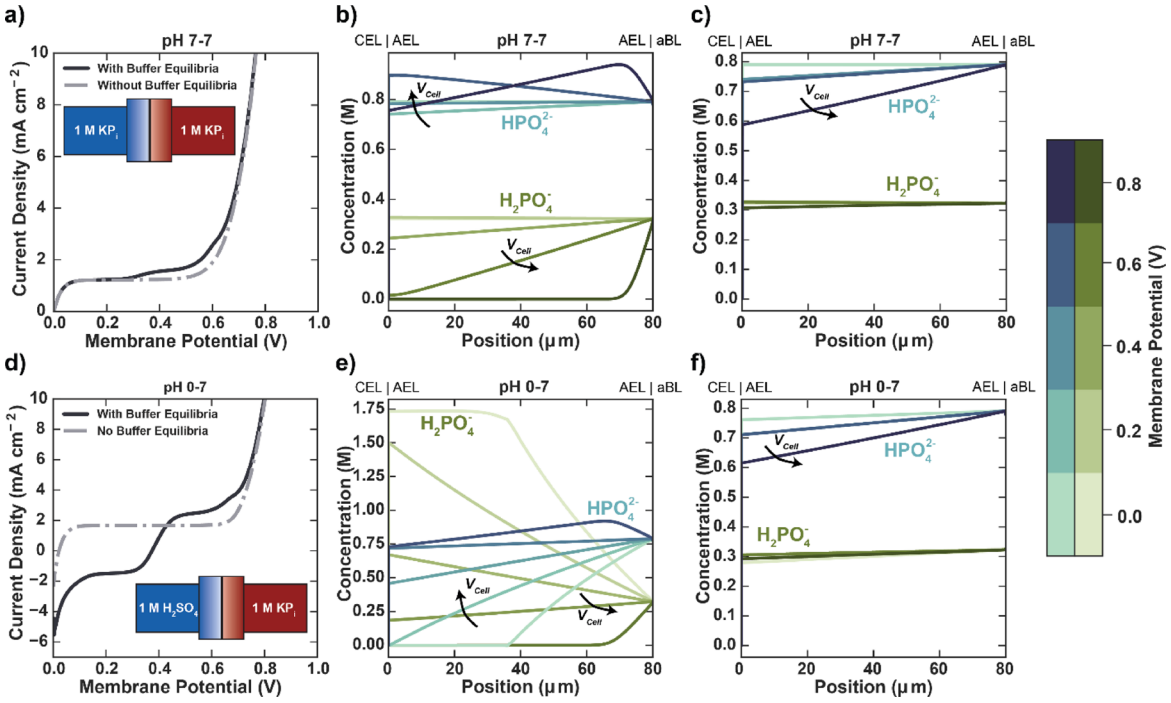

Figure 8. Polarization curves (a, d) and AEL phosphate concentration profiles with (b, e) and without (c, f) buffer equilibria for (a–c) pH 7-7 and (d–f) pH 0-7. Arrows represent the direction of increasing membrane voltage.

and 10 nm.[31] This is shown in the simulated profiles (Figure 7). The double layer is initially thinner than the catalyst layer, but as the applied potential increases, the thickness of the double layer grows and eventually surpasses the catalyst layer thickness. Notably, the concentration peak for hydroxide in the double layer is larger than that for hydronium. This is again due to the low diffusivity of hydroxide ions as the hydronium ions can diffuse away from the double layer more rapidly. Interestingly, Figure 5 reveals that the hydronium and hydroxide concentrations can reach values of ∼1.85 M, exceeding the fixed-charge concentration of 1.81 M. This discrepancy is caused by the preservation of electroneutrality in the presence of salt ions outside of the double layer. Therefore, these profiles are not only a function of the transport properties of hydronium and hydroxide ions but also a function of other ions in the system. This finding reinforces the significance of understanding co- and counter-ion transport when modeling BPMs.

It is important to note the unique behavior of BPMs at zero applied membrane potential (i.e., an applied bias of 0 V across the membrane) in the pH 0-7, pH 7-14, and pH 0-14 cases. For these three cases, at zero applied membrane potential, there are measured negative currents of −4, −2, and −260 mA cm^{-2} (see Figure S13 in the Supporting Information), respectively. At these negative currents, hydroxide and hydronium ions move toward the junction, and recombination will occur due to mass action. For the pH 0-7 case, this recombination rate is limited by the low concentration of hydroxide ions in the junction, and hydronium ions from the fully exchanged CEL appear in excess. Conversely, for the pH 7-14 case, the recombination rate is limited by the low concentration of hydronium ions, and hydroxide ions from the fully exchanged AEL appear in excess. In both cases, the species that appears in excess can cross through the junction because it is not completely consumed in the reaction, explaining the observed crossover in the concentration profiles at zero applied membrane potential. For the pH 0-14 case, at zero applied membrane potential, the recombination current is very high, and as shown in Figure S13, within a mass-transport-limited regime. Both the CEL and AEL are fully exchanged with hydronium and hydroxide, respectively, but because hydronium transports faster than hydroxide, it appears in slight excess in the junction, and large hydroxide concentration gradients form (see Figure 5d) within the AEL due to its slower transport. All behaviors observed at little-to-no applied membrane potential are eliminated as the applied potential is increased and the current direction reverses, evacuating the junction and reducing the rate of recombination due to mass action.

3.4. Salt-Ion Transport and Impact of Buffer. To maintain steady pH gradients for electrolysis and improve membrane functionality, a complete understanding of how co- and counter-ions affect transport in a BPM is necessary. Several investigators have commented on the factors affecting co- and counter-ion transport. For example, Blommaert *et al.*[5] demonstrated that co- and counter-ion transport are affected by the equilibrium constant of the buffer reactions of the electrolyte species. Additionally, for other applications such as CO_2 electrolysis, which involves similar applied pH gradients, the electrolyte salt ions have been shown to have an impact on the reaction selectivity, with larger electrolyte cations suppressing HER and improving CO_2-reduction selectivity.[62] Therefore, optimizing the choice of the electrolyte salt to maximize reaction efficiency and BPM performance is critical.

Insights into co- and counter-ion transport can be made by an analysis of species concentration profiles. At increased membrane potentials where breakdown occurs, the counter-ion profiles are opposite to those for hydronium and hydroxide ions and serve to maintain electroneutrality (Figures S14–S16 in the Supporting Information). For a reverse-bias BPM, the counter-ions are in greatest concentration near the electrolyte due to Donnan effects and are minimal near the AEL/CEL

https://dx.doi.org/10.1021/acsami.0c12686
ACS Appl. Mater. Interfaces 2020, 12, 52509–52526

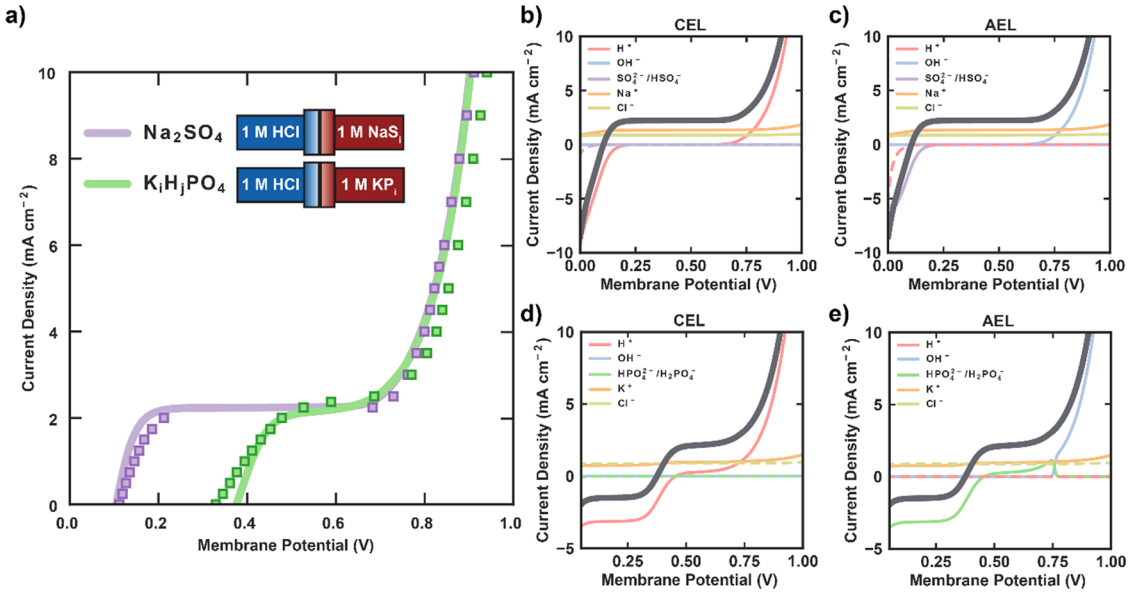

Figure 9. (a) Simulated (solid lines) and experimental (markers) polarization curves for pH 0-7 1 M HCl | 1 M Na_2SO_4 and 1 M HCl | 1 M $K_iH_jPO_4$ electrolytes. Partial-current-density breakdown in the (b) CEL and (c) AEL for a 1 M HCl | 1 M Na_2SO_4 submersed BPM. Partial current density breakdown in the (d) CEL and (e) AEL for a 1 M HCl | 1 M $K_iH_jPO_4$ submersed BPM.

junction where water dissociation occurs. Co-ions, on the other hand, are not as readily absorbed into the BPM due to Donnan exclusion and are thus present at low concentrations throughout the membrane.

While homogeneous buffer reactions are frequently neglected in models of BPMs, their impact must be considered. This is especially true in the pH 7-7 and pH 0-7 cases, for which the phosphate anions are strongly absorbed into the BPM due to direct contact of the phosphate-containing electrolyte with the AEL. For these environments, the AEL is initially saturated with phosphate species, and the buffer kinetics significantly affect the concentration profiles of the salt ions and the electrochemical characteristics of the BPM. Figure 8 shows the polarization curves and AEL phosphate species profiles for the pH 7-7 and pH 0-7 cases with and without consideration of the homogeneous buffer equilibria for applied voltages within the salt-ion-crossover regime. The polarization curves (Figure 8a,d) exhibit significant changes when the homogeneous reaction equilibria are considered. Namely, the formation of a secondary plateau current is achieved when buffer equilibria are included in the model. Reference to the analysis of the partial current densities in the AEL presented in Figure 4 demonstrates that current in the plateau region is carried primarily by the phosphate (green) species. This is further supported by examining the concentration profiles (Figure 8b,e), where analysis of phosphate species concentration in the AEL reveals profiles that can explain the secondary plateau in the observed current. As the membrane potential is increased, hydroxide anions form within the catalyst layer and are transported into the AEL, thereby shifting the equilibrium between hydrogen phosphate and dihydrogen phosphate toward hydrogen phosphate (eq 10). This shift decreases the concentration of hydrogen phosphate and increases the concentration of dihydrogen phosphate in the AEL. As shown in Figure 8c,f, when the buffer reactions are ignored, the concentration profiles within the AEL for phosphate remain linear, and no titration current is observed. Hence, to describe co- and counter-ion transport in a BPM fully, the homogeneous reaction equilibria must be considered.

Because the buffer equilibria affect BPM performance significantly, the choice of the anolyte species, which contains anions that readily transport into the AEL and undergo homogeneous reactions, is very important for developing a BPM-electrolyzer. To characterize the impact of the choice of anolyte species, polarization curves and partial current densities were analyzed for two additional electrolyte environments: 1 M HCl | 1 M Na_2SO_4 and 1 M HCl | 1 M $K_iH_jPO_4$ (Figure 9). The experimental methodology for the measurement of these polarization curves through four-probe experiment and schematic (Figure S7) is given in Section S6 of the Supporting Information. These curves were fit using approximately the same fitting parameters used to fit the data of Vermaas *et al.*,[4] except for very slight changes in the value of q (1.0 for Vermaas *et al.* to 1.1 for our data) and the catalyst effectiveness factor (1.8 for Vermaas *et al.* to 1.6 for our data) (see Table S4). Notably, in the measurement of these polarization curves, the voltage at each applied current density was not recorded until the voltage stabilized to capture fully the steady-state behavior of the BPM (see Figure S8). In both cases, the pH environment of the catholyte is 0 and that of the anolyte is 7. These electrolytes were chosen because, as shown in Figure 8, the current generated by titration for this pH environment is higher than for the pH 7-7 environment. The polarization curves for the two electrolyte combinations demonstrate that the choice of anolyte has a significant impact on the electrochemical characteristics of the BPM. While the kinetics of the water dissociation seem largely unaffected, and the magnitude of the salt-ion leakage currents are essentially identical, there is an observable difference in the open-circuit potential (OCP) of the two polarization curves. This is likely due to internal buffering within the bipolar membrane, as evidenced by the significant negative partial current densities of the buffered phosphate and sulfate species that can be attributed to titration currents. This is further supported by the fact that the OCPs in these two cases are proportional to

https://dx.doi.org/10.1021/acsami.0c12686
ACS Appl. Mater. Interfaces 2020, 12, 52509−52526

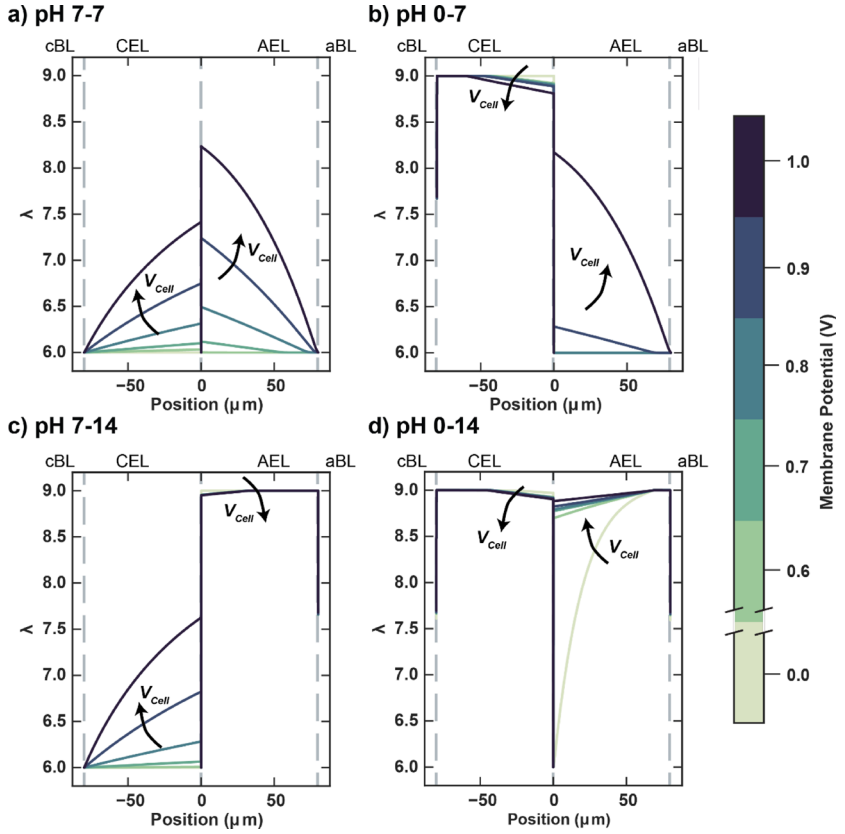

Figure 10. Water-content profiles at various applied potentials for four modeled pH environments: (a) pH 7-7, (b) pH 0-7, (c) pH 7-14, and (d) pH 0−14. Arrows represent the direction of increasing membrane potential.

the pK_a of their respective buffer species. Further research should vary buffer species systematically over a variety of applied pH gradients to examine fully the impact of the pK_a on the OCP of the BPM.

3.5. Water Concentration Gradients. Controlling water transport within a BPM is critical to minimizing degradation of BPM-electrolyzer performance due to possible layer delamination caused by dehydration of the AEL/CEL junction at high current densities.[25,29,63] Therefore, maximizing BPM lifetime and performance requires knowledge of the water content and gradients in a BPM, something that has not previously been explored.[23,38] Prior studies by Crothers *et al.*[21] and Peng *et al.*[60] have demonstrated how ionomer hydration depends on the fraction of absorbed salt ions in a cationic-exchange or an anionic-exchange membrane. Because of differences in osmotic pressure, as the fraction of co- or counter-ions in the membrane increases, the membrane takes up less water.[21] In other words, the salt-ion-exchanged form of the AEL or CEL will take up less water than its corresponding hydronium or hydroxide form. Work by Crothers *et al.*[21] has demonstrated that, for most salt ions, the profile of hydration as a function of hydronium fraction in the CEL is approximately linear. Therefore, by fitting a value for the hydration of the AEL and CEL when completely exchanged with salt ions ($\lambda_{f_{H_3O^+}=0}$, $\lambda_{f_{OH^-}=0}$), the linear profile (eqs 34 and 35) defining local ionomer hydration as a function of hydroxide or hydronium fraction captures approximately the decreased affinity for water in the two membranes with increasing salt-ion uptake.

When concentration polarization is achieved in a BPM at high membrane potential in contact with a neutral electrolyte, there will be a distinct change in the majority carrier in the ion-exchange layer as the AEL/CEL junction is approached. Near the ionomer layer/electrolyte interfaces, the ionic concentration in the membrane is defined by Donnan equilibrium with the electrolyte, and the membrane strongly takes up salt ions. However, near the AEL/CEL interface where dissociation occurs, the ion-exchange layers are exchanged by hydronium or hydroxide ions, respectively, due to local generation of these ions at high membrane potentials. Because membrane hydration depends on the specific ionic content of the membrane, the level of hydration is not uniform throughout the membrane, and there are internal gradients in water concentration (Figure 10). It is critical to capture these concentration gradients when modeling multi-ion transport because, as shown previously in Figure 6, they result in a non-negligible driving force for ionic current within the BPM. Also, sharp gradients in membrane hydration at the interface (see Figure S17 in the Supporting Information) could lead to nonuniform swelling in the BPM that could, in turn, explain delamination due to dehydration.[20,61,64] Since the description of water transport within a BPM is incomplete, further work should seek to define more completely the effects of individual co- and counter-ions on membrane hydration. Also needed is a more thorough understanding of water transport through the membrane in order to understand more fully the factors affecting membrane dry-out and delamination of BPMs.

3.6. Sensitivity Analysis. Although BPMs present great promise for application in electrolysis, until recently, they were primarily used for the generation of acid and base,[23,65,66] and, hence, there are only a handful of studies devoted to the design of next-generation BPMs for electrochemical technologies

https://dx.doi.org/10.1021/acsami.0c12686
ACS Appl. Mater. Interfaces 2020, 12, 52509−52526

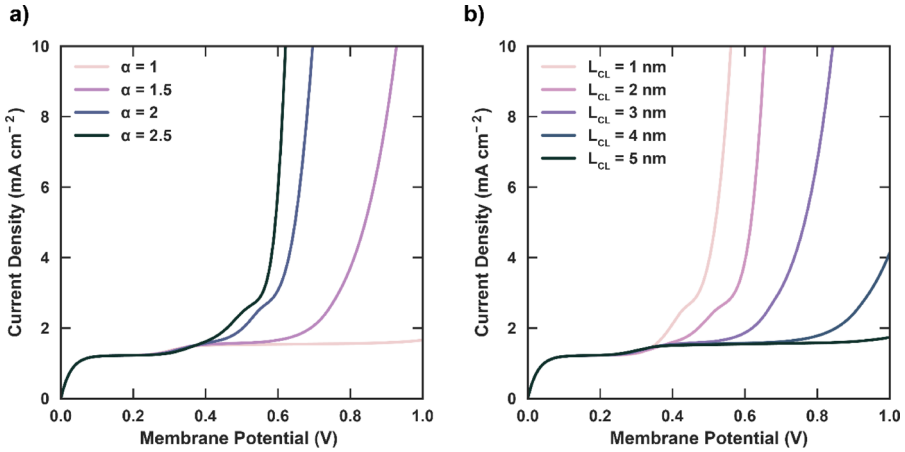

Figure 11. Modeled polarization curve for pH 7-7 for various (a) catalyst effectiveness factors and (b) catalyst-layer thicknesses. Fitted values for the BPM in the current study are L_{CL} = 2.7 nm and α = 1.8. (See Table S3).

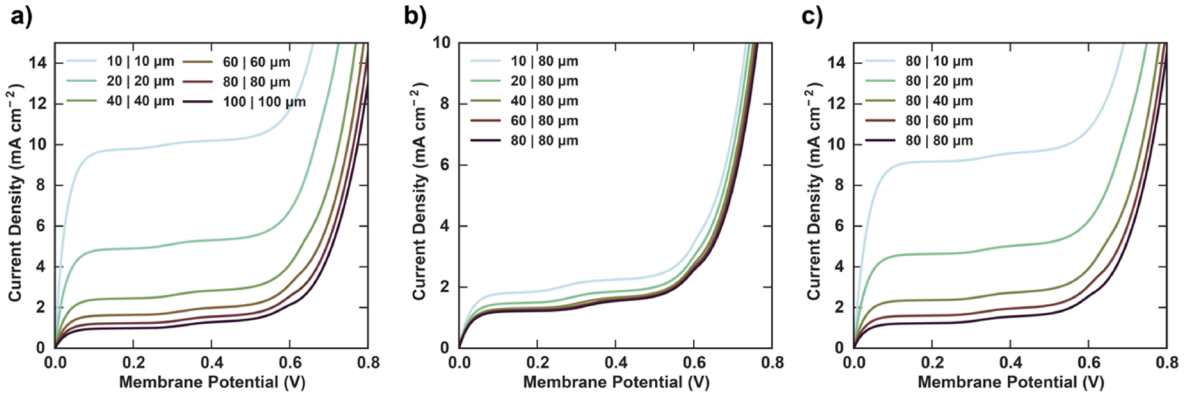

Figure 12. Effect of modifying BPM membrane thickness (a) symmetrically, (b) of just the CEL, and (c) of just the AEL. Membrane used in study was symmetric with an 80 μm CEL and an 80 μm AEL.

including electrolyzers.[25,26,33] With this end in mind, we define two main objectives. First, the BPM must be able to achieve high current densities of water dissociation for minimal applied potentials. Second, the BPM should operate with minimal salt-ion crossover in order to maintain a stable pH gradient during extended operation. Using the developed model, we assess the parameter space for BPM design and provide recommendations for novel BPMs that are optimized for electrolysis. The sensitivity analysis discussed below was performed for the pH 7-7 polarization curve because it has the clearest delineation between the salt-ion crossover and water-dissociation regimes, enabling clearer visualization of the impact of the changes in parameters on co- and counter-ion leakage and water-dissociation kinetics. Increases in the current in the plateau region of these polarization curves are undesirable and can be attributed to salt-ion crossover and increases in current in the WD region are beneficial and correspond to enhanced water-dissociation kinetics. Additionally, the low current densities simulated in this study are relevant for solar water splitting applications in similar near-neutral conditions. Furthermore, trends discovered for pH 7-7 translate well to the other pH gradients.

To achieve high water-dissociation current densities at lower applied potentials, it is necessary to optimize the water-dissociation catalysts in the BPM catalyst layer. In the current study, there are two parameters that control the behavior of the water-dissociation catalyst: the catalyst-layer thickness, and the catalyst effectiveness factor, α. Figure 11 shows the sensitivity of the model to these parameters. As shown in Figure 11a, a higher value of α and a thinner catalyst layer both decrease the onset potential required for breakdown and exhibit steeper slopes approaching the water-dissociation current density. By increasing α, the free energy of Bjerrum dipole is reduced and dissociation can occur more readily. Additionally, by decreasing the thickness of the catalyst layer, the catalyst is placed and utilized only near the center of the BPM, where the electric field is at its maximum. This increase in efficient utilization of the catalyst is responsible for the improvement in performance with a thinner catalyst layer, consistent with previous modeling studies.[38] Comparison to the values fit to the experimental data, L_{CL} = 2.7 nm and α = 1.8 (see Table S3), demonstrates that there is room for improvement in the design of thinner, more effective water-dissociation catalyst layers, and Figure 11 shows that the greatest opportunity for improvement is in using thinner catalyst layers.

At the high current densities required for commercial electrolysis (>100 mA/cm^2),[1] the ohmic resistances in the membrane can lead to significant voltage losses. Therefore, it is desirable to reduce the thickness of the BPM in order to minimize ohmic overpotential losses at high water-dissociation current densities. However, reducing the thickness of the BPM will in turn increase the salt-ion leakage and reduce the stability of the applied pH gradient. Therefore, there is a trade-off between ohmic losses and salt-ion leakage. This trade-off is

https://dx.doi.org/10.1021/acsami.0c12686
ACS Appl. Mater. Interfaces 2020, 12, 52509−52526

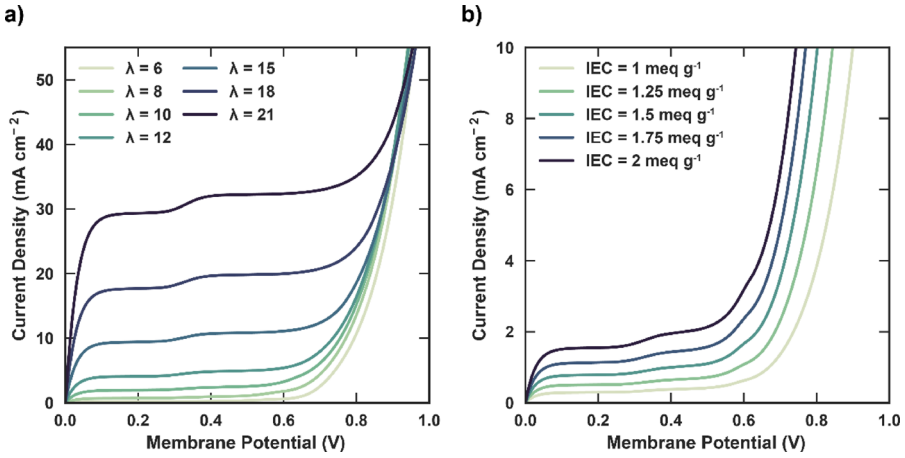

Figure 13. Effect of modifying (a) BPM hydration and (b) ion-exchange capacity. BPM hydration in study had a λ of 9 and an IECs of 1.81 meq g^{-1}.

relevant to many electrochemical technologies[67] and needs to be further explored for BPM devices. The effect of membrane thickness on the current/potential-characteristics of the BPM is shown in Figure 12. As expected, the co- and counter-ion leakage current observed increases with decreased membrane thickness. However, as evidenced by Figure 12b,c, the thickness of the AEL dictates the magnitude of the salt-ion leakage, and the model is relatively insensitive to changes in the thickness of the CEL. Additionally, it is seen that the effects of decreasing the AEL and CEL independently are linearly additive (i.e., the sum of the change in leakage in Figure 12b,c equals the change in leakage in Figure 12a). This implies that the most effective BPM would be one with as thin a CEL as possible supported on a thicker AEL in order to keep salt-ion leakage low and membrane conductance high while maintaining mechanical integrity. This type of asymmetric BPM-structure has been proposed for BPM CO_2 electrolysis, where a thinner, porous CEL allows for any CO_2 gas formed at the AEL/CEL junction to permeate back to the cathode where it could be utilized.[29]

The last set of parameters that can be optimized in the BPM are those related to the physical properties of the ionomer layers: the membrane water uptake and the IEC. These are related in that the water uptake increases with IEC for ionomers.[20,68] Nonetheless, for the purposes of the sensitivity analysis, it is elucidating to modulate them separately. Prior studies have shown that the Fumasep BPMs exhibit drastically lower water uptake (λ = 9)[5] than commercial monopolar membranes like Nafion (λ = 21)[61,69] or Tokuyama A201 (λ = 17) .[60] For these monopolar membranes, there is an incentive to maximize water uptake in order to improve conductivity and prevent membrane dehydration. However, BPMs face another trade-off. As shown in Figure 13a, increased water uptake severely increases salt-ion leakage due to the dependence on the transport coefficients of the salt ions on the water content within the BPM. At the Nafion hydration of 21, the BPM exhibits a significant (~30 mA cm^{-2}) of co- and counter-ion leakage current. Therefore, the high hydration of commercial monopolar membranes will be undesirable in the fabrication of BPMs; consequently, further work should seek to find an optimum balance between membrane hydration and salt-ion leakage. When exploring methods to minimize crossover current and membrane resistance in the context of redox flow batteries, Crothers *et al.* found that one approach to achieving optimum performance was to change the transport coefficient or uptake of ions in the membrane by making the redox species much larger or to change the membrane pore size to more closely match the size of the redox species to leverage size-exclusion properties.[67] Future modeling efforts should attempt to capture size-exclusion effects and membrane/species interactions in order to study the sensitivity of salt-ion crossover to these parameters.

While the effect of increased water uptake is quite straightforward, the impact of increasing IEC, which characterizes the amount of membrane fixed-charge groups per gram of membrane, is complex. In Figure 13b, it is observed that as the IEC is increased, the salt-ion leakage increases, a result that is detrimental to performance, but the applied potential required for breakdown is reduced, implying an improvement in water-dissociation kinetics. Both effects are coupled to the increase in fixed-charge concentration in the membrane that corresponds to an increase in the IEC. As the fixed-charge concentration increases, the water uptake and number of co-ions that transport into the membrane by Donnan equilibrium increases, leading to an increase in co-ion leakage. Additionally, increasing IEC could lead to higher likelihood of polymer dissolution.[20] At the same time, increasing the magnitude of fixed charges in each exchange layer increases the gradient in fixed-charge density at the AEL/CEL junction, leading to a larger local electric field and thus enhanced water dissociation for higher IECs due to the Second Wien Effect. The coupled sensitivity of the IEC to enhancements in water dissociation and increases in co- and counter-ion leakage makes it difficult to optimize the IEC for a BPM. Since the sensitivity of the salt-ion leakage current is minimal, the electric-field enhancement will likely be more critical to defining the BPM performance at high current densities desired for electrolysis.[1,5] Therefore, it is sensible to maximize the IEC in order to enhance interfacial water dissociation, although there is an intrinsic limit where the ionomer will dissolve at high enough IECs.

4. CONCLUSIONS

A comprehensive model for a bipolar membrane (BPM) operated in reverse bias was developed and validated against experimental data. The model accounts for the effects of multi-ion transport, homogeneous reaction kinetics, electric field-dependent water dissociation, and catalyzed water-dissociation kinetics. Simulations based on this model describe previously

https://dx.doi.org/10.1021/acsami.0c12686
ACS Appl. Mater. Interfaces 2020, 12, 52509−52526

unexplained electrochemical phenomena such as internal concentration polarization and salt-ion crossover that are critical for developing energy efficient and pH stable BPM-electrolyzers. The model also demonstrates several important phenomena central to multi-ion transport within the BPM. In particular, the simulations reveal that co- and counter-ion currents dominate at low current densities, that there is a distinct change in the mode of transport between diffusion for a BPM in a neutral electrolyte and migration for a BPM in a highly alkaline or acidic electrolyte, and that the buffer kinetics of the electrolyte salt ions are vital for describing co- and counter-ion crossover fully in a BPM. Lastly, the model demonstrates the sensitivity of BPM performance to the catalyst-layer properties and physical properties of the ion-exchange layers. The simulations show that an optimal BPM should have a thin dissociation catalyst layer, and a thinner AEM than CEM layer in order to manage water transport, control salt-ion crossover, and ameliorate ohmic resistance. The work reported also identifies areas for improving the accuracy of the model for a BPM. These include capturing concentrated-solution effects, membrane/species interactions, and solving explicitly for water transport. These phenomena will become especially relevant at current densities higher than those currently measured experimentally but relevant for device operation. Nevertheless, the results of the present study provide information that is critical to developing a comprehensive understanding of multi-ion transport in BPMs and informs the design and implementation of BPMs in next-generation devices for various electrochemical reactions that benefit from operation under an applied pH gradient.

■ ASSOCIATED CONTENT

Supporting Information

The Supporting Information is available free of charge at https://pubs.acs.org/doi/10.1021/acsami.0c12686.

Model Sensitivity to Electrolyte Boundary Layer Thickness and Mesh, Derivation of Equilibrium Constants in a Molar Ratio Reference, Membrane Fixed-Charge Distribution, Donnan Equilibrium between Membrane and Electrolyte, Membrane Hydration Hydronium/Hydroxide Content Dependence, Experimental Methods for Four-Probe Measurement, Model Equation Set, Fitting Parameter Tables, Plot of H_3O^+/OH^- Fraction of Current, Electrostatic Potential Profiles, Interfacial Electric Fields, Simplified Counterion Concentration Profiles, Complete Counterion Concentration Profiles, and Depletion Region Hydration Profiles (PDF)

■ AUTHOR INFORMATION

Corresponding Author

Adam Z. Weber − *Joint Center for Artificial Photosynthesis, Lawrence Berkeley National Laboratory, Berkeley, California 94720, United States;* orcid.org/0000-0002-7749-1624; Phone: (510) 486-6308; Email: azweber@lbl.gov

Authors

Justin C. Bui − *Department of Chemical and Biomolecular Engineering, University of California Berkeley, Berkeley, California 94720, United States; Joint Center for Artificial Photosynthesis, Lawrence Berkeley National Laboratory, Berkeley, California 94720, United States;* orcid.org/0000-0003-4525-957X

Ibadillah Digdaya − *Joint Center for Artificial Photosynthesis, California Institute of Technology, Pasadena, California 91125, United States*

Chengxiang Xiang − *Joint Center for Artificial Photosynthesis, California Institute of Technology, Pasadena, California 91125, United States;* orcid.org/0000-0002-1698-6754

Alexis T. Bell − *Department of Chemical and Biomolecular Engineering, University of California Berkeley, Berkeley, California 94720, United States; Joint Center for Artificial Photosynthesis, Lawrence Berkeley National Laboratory, Berkeley, California 94720, United States;* orcid.org/0000-0002-5738-4645

Complete contact information is available at: https://pubs.acs.org/10.1021/acsami.0c12686

Notes

The authors declare no competing financial interest.

■ ACKNOWLEDGMENTS

This material is based on work performed at the Joint Center for Artificial Photosynthesis, a DOE Energy Innovation Hub, supported through the Office of Science of the U.S. Department of Energy under award number DE-SC0004993 and the National Institutes of Health under grant no. S10OD023532. J.C.B. acknowledges funding from the National Science Foundation Graduate Research Fellowship under grant no. DGE 1752814. The authors would also like to thank David Vermaas, Philomena Weng, and Andrew Crothers for insightful and fruitful discussions regarding the nature of ionic transport in bipolar membranes.

■ NOMENCLATURE

Roman

c_i, concentration of species i (M)
D_i, diffusivity of species i ($m^2\ s^{-1}$)
E, electric field ($V\ m^{-1}$)
E, elementary charge
F, Faraday constant
G, Gibbs free energy ($J\ mol^{-1}$)
IEC, ion exchange capacity ($mmol\ g^{-1}$)
k_B, Boltzmann constant
K_n, equilibrium constant in reaction n
K_n, forward rate constant of reaction n
L, length (m)
l_B, Bjerrum length (m)
M_i, molar mass of species i ($g\ mol^{-1}$)
N_i, molar flux of species i ($mol\ m^{-2}\ s^{-1}$)
R, ideal gas constant
R_i, source term for species i ($mol\ m^{-3}\ s^{-1}$)
$s_{i,n}$, stoichiometric coefficient of species i in reaction n
T, temperature (K)
x, one-dimensional position variable (m)
z_i, charge of ion i

Greek

α, catalyst effectiveness factor
β, non-dimensional electric field
γ_i, activity coefficient of species i
ε, dielectric permittivity ($F\ m^{-1}$)
λ, water content
μ_i, chemical potential of species i ($J\ mol^{-1}$)
ξ, species-membrane/species-water diffusivity ratio
ρ, density ($g\ cm^{-3}$)

https://dx.doi.org/10.1021/acsami.0c12686
ACS Appl. Mater. Interfaces 2020, 12, 52509−52526

σ, dimensionless dissociation bond length
Φ, electrostatic potential (V)
ϕ, ionomer water volume fraction

Subscript

−, hydroxide species
+, hydronium species
char, characteristic
eff, effective
i, ionic species
w, value in water

Superscript

0, intrinsic value or standard state
E, electric field dependence

Acronyms

aBL, anolyte boundary layer
AEL, anion exchange layer
BPM, bipolar membrane
cBL, catholyte boundary layer
CEL, cation exchanger layer
CL, catalyst layer
DL, double layer

REFERENCES

(1) Barbir, F. PEM Electrolysis for Production of Hydrogen from Renewable Energy Sources. *Sol. Energy* **2005**, *78*, 661−669.
(2) Blanco, D. E.; Modestino, M. A. Organic Electrosynthesis for Sustainable Chemical Manufacturing. *Trends Chem.* **2019**, *1*, 8−10.
(3) Salvatore, D. A.; Weekes, D. M.; He, J.; Dettelbach, K. E.; Li, Y. C.; Mallouk, T. E.; Berlinguette, C. P. Electrolysis of Gaseous CO_2 to CO in a Flow Cell with a Bipolar Membrane. *ACS Energy Lett.* **2018**, *3*, 149−154.
(4) Vermaas, D. A.; Wiegman, S.; Nagaki, T.; Wilson, A. S. Ion Transport Mechanisms in Bipolar Membranes for (Photo)-Electrochemical Water Splitting. *Sustainable Energy Fuels* **2018**, 2006−2015.
(5) Blommaert, M. A.; Verdonk, J. A. H.; Blommaert, H. C. B.; Smith, W. A.; Vermaas, D. A. Reduced Ion Crossover in Bipolar Membrane Electrolysis via Increased Current Density, Molecular Size and Valence. *ACS Appl. Energy Mater.* **2020**, 5804.
(6) Vermaas, D. A.; Smith, W. A. Synergistic Electrochemical CO_2 Reduction and Water Oxidation with a Bipolar Membrane. *ACS Energy Lett.* **2016**, *1*, 1143−1148.
(7) Shaner, M. R.; Atwater, H. A.; Lewis, N. S.; McFarland, E. W. A Comparative Technoeconomic Analysis of Renewable Hydrogen Production Using Solar Energy. *Energy Environ. Sci.* **2016**, *9*, 2354−2371.
(8) McCrory, C. C. L.; Jung, S.; Ferrer, I. M.; Chatman, S. M.; Peters, J. C.; Jaramillo, T. F. Benchmarking Hydrogen Evolving Reaction and Oxygen Evolving Reaction Electrocatalysts for Solar Water Splitting Devices. *J. Am. Chem. Soc.* **2015**, *137*, 4347−4357.
(9) Lazouski, N.; Chung, M.; Williams, K.; Gala, M. L.; Manthiram, K. Non-Aqueous Gas Diffusion Electrodes for Rapid Ammonia Synthesis from Nitrogen and Water-Splitting-Derived Hydrogen. *Nat. Catal.* **2020**, *3*, 463.
(10) Blanco, D. E.; Dookhith, A. Z.; Modestino, M. A. Enhancing Selectivity and Efficiency in the Electrochemical Synthesis of Adiponitrile. *React. Chem. Eng.* **2019**, *4*, 8−16.
(11) Blanco, D. E.; Prasad, P. A.; Dunningan, K.; Modestino, M. A. Insights into Membrane-Separated Organic Electrosynthesis: The Case of Adiponitrile Electrochemical Production. *React. Chem. Eng.* **2020**, *5*, 136−144.
(12) Bagherzadeh Mostaghimi, A. H.; Al-Attas, T. A.; Kibria, M. G.; Siahrostami, S. A Review on Electrocatalytic Oxidation of Methane to Oxygenates. *J. Mater. Chem. A* **2020**, 15575.
(13) Kumari, S.; Turner White, R.; Kumar, B.; Spurgeon, J. M. Solar Hydrogen Production from Seawater Vapor Electrolysis. *Energy Environ. Sci.* **2016**, *9*, 1725−1733.
(14) Luo, J.; Vermaas, D. A.; Bi, D.; Hagfeldt, A.; Smith, W. A.; Grätzel, M. Bipolar Membrane-Assisted Solar Water Splitting in Optimal PH. *Adv. Energy Mater.* **2016**, *6*, 1−7.
(15) Oener, S. Z.; Ardo, S.; Boettcher, S. W. Ionic Processes in Water Electrolysis: The Role of Ion-Selective Membranes. *ACS Energy Lett.* **2017**, *2*, 2625−2634.
(16) Li, Y. C.; Zhou, D.; Yan, Z.; Gonçalves, R. H.; Salvatore, D. A.; Berlinguette, C. P.; Mallouk, T. E. Electrolysis of CO_2 to Syngas in Bipolar Membrane-Based Electrochemical Cells. *ACS Energy Lett.* **2016**, *1*, 1149−1153.
(17) Xiang, C.; Papadantonakis, K. M.; Lewis, N. S. Principles and Implementations of Electrolysis Systems for Water Splitting. *Mater. Horizons* **2016**, *3*, 169−173.
(18) Sun, K.; Liu, R.; Chen, Y.; Verlage, E.; Lewis, N. S.; Xiang, C. A Stabilized, Intrinsically Safe, 10% Efficient, Solar-Driven Water-Splitting Cell Incorporating Earth-Abundant Electrocatalysts with Steady-State pH Gradients and Product Separation Enabled by a Bipolar Membrane. *Adv. Energy Mater.* **2016**, 1−7.
(19) Mcdonald, M. B.; Ardo, S.; Lewis, N. S.; Freund, M. S. Use of Bipolar Membranes for Maintaining Steady-State pH Gradients in Membrane-Supported , Solar-Driven Water Splitting. *ChemSusChem* **2014**, 3021−3027.
(20) Kusoglu, A.; Weber, A. Z. New Insights into Perfluorinated Sulfonic-Acid Ionomers. *Chem. Rev.* **2017**, *117*, 987−1104.
(21) Crothers, A. R.; Darling, R. M.; Kusoglu, A.; Radke, C. J.; Weber, A. Z. Theory of Multicomponent Phenomena in Cation-Exchange Membranes: Part I. Thermodynamic Model and Validation. *J. Electrochem. Soc.* **2020**, *167*, No. 013547.
(22) Kutz, R. B.; Chen, Q.; Yang, H.; Sajjad, S. D.; Liu, Z.; Masel, I. R. Sustainion Imidazolium-Functionalized Polymers for Carbon Dioxide Electrolysis. *Energy Technol.* **2017**, *5*, 929−936.
(23) Craig, N. P. Electrochemical Behavior of Bipolar Membranes. Ph.D. Dissertation, University of California, Berkeley, Berkeley, CA, 2013.
(24) Oener, S. Z.; Foster, M. J.; Boettcher, S. W. Accelerating Water Dissociation in Bipolar Membranes and for Electrocatalysis. *Science* **2020**, *369*, 1099.
(25) Shen, C.; Wycisk, R.; Pintauro, P. N. High Performance Electrospun Bipolar Membrane with a 3D Junction. *Energy Environ. Sci.* **2017**, *10*, 1435−1442.
(26) McDonald, M. B.; Freund, M. S.; Hammond, P. T. Catalytic, Conductive Bipolar Membrane Interfaces through Layer-by-Layer Deposition for the Design of Membrane-Integrated Artificial Photosynthesis Systems. *ChemSusChem* **2017**, *10*, 4599−4609.
(27) McDonald, M. B.; Bruce, J. P.; McEleney, K.; Freund, M. S. Reduced Graphene Oxide Bipolar Membranes for Integrated Solar Water Splitting in Optimal pH. *ChemSusChem* **2015**, *8*, 2645−2654.
(28) Gabrielsson, E. O.; Tybrandt, K.; Berggren, M. Ion Diode Logics for pH Control. *Lab Chip* **2012**, *12*, 2507−2513.
(29) Pătru, A.; Binninger, T.; Pribyl, B.; Schmidt, T. J. Design Principles of Bipolar Electrochemical Co-Electrolysis Cells for Efficient Reduction of Carbon Dioxide from Gas Phase at Low Temperature. *J. Electrochem. Soc.* **2019**, *166*, F34−F43.
(30) White, W.; Sanborn, C. D.; Fabian, D. M.; Ardo, S. Conversion of Visible Light into Ionic Power Using Photoacid-Dye-Sensitized Bipolar Ion-Exchange Membranes. *Joule* **2018**, *2*, 94−109.
(31) Mafé, S.; Ramíaz, P. Electrochemical Characterization of Polymer Ion-Exchange Bipolar Membranes. *Acta Polym.* **1997**, *48*, 234−250.
(32) Mafé, S.; Ramírez, P.; Alcaraz, A. Electric Field-Assisted Proton Transfer and Water Dissociation at the Junction of a Fixed-Charge Bipolar Membrane. *Chem. Phys. Lett.* **1998**, *294*, 406−412.
(33) McDonald, M. B.; Freund, M. S. Graphene Oxide as a Water Dissociation Catalyst in the Bipolar Membrane Interfacial Layer. *ACS Appl. Mater. Interfaces* **2014**, *6*, 13790−13797.

https://dx.doi.org/10.1021/acsami.0c12686
ACS Appl. Mater. Interfaces 2020, 12, 52509−52526

(34) Yan, Z.; Zhu, L.; Li, Y. C.; Wycisk, R. J.; Pintauro, P. N.; Hickner, M. A.; Mallouk, T. E. The Balance of Electric Field and Interfacial Catalysis in Promoting Water Dissociation in Bipolar Membranes. *Energy Environ. Sci.* **2018**, *11*, 2235−2245.
(35) Vermaas, D. A.; Sassenburg, M.; Smith, W. A. Photo-Assisted Water Splitting with Bipolar Membrane Induced PH Gradients for Practical Solar Fuel Devices. *J. Mater. Chem. A* **2015**, *3*, 19556−19562.
(36) Oener, S. Z.; Foster, M. J.; Boettcher, S. W. Accelerating Water Dissociation in Bipolar Membranes and for Electrocatalysis. *Science* **2020**, No. eaaz1487.
(37) Volgin, V. M.; Davydov, A. D. Ionic Transport through Ion-Exchange and Bipolar Membranes. *J. Memb. Sci.* **2005**, *259*, 110−121.
(38) Mareev, S. A.; Evdochenko, E.; Wessling, M.; Kozaderova, O. A.; Niftaliev, S. I.; Pismenskaya, N. D.; Nikonenko, V. V. A Comprehensive Mathematical Model of Water Splitting in Bipolar Membranes: Impact of the Spatial Distribution of Fixed Charges and Catalyst at Bipolar Junction. *J. Memb. Sci.* **2020**, *603*, 118010.
(39) Fumatech. *Technical Data Sheet for Fumasep FBM*. 2020.
(40) U.S. Geological Survey. *PHREEQC (Version 3) - A Computer Program for Speciation, Batch-Reaction, One-Dimensional Transport, and Inverse Geochemical Calculations*.
(41) Zumdahl, S.; DeCoste, D. *Chemical Principles*, 8th ed.; Cengage Learning: Boston, MA, 2016, Appendix 5, A22.
(42) Eigen, M. Proton Transfer, Acid-Base Catalysis, and Enzymatic Hydrolysis. *Angew. Chemie* **1964**, *3*, 1−19.
(43) Kaiser, V.; Bramwell, S. T.; Holdsworth, P. C. W.; Moessner, R. Onsager's Wien Effect on a Lattice. *Nat. Mater.* **2013**, *12*, 1033−1037.
(44) Kaiser, V. The Wien Effect in Electric and Magnetic Coulomb Systems - from Electrolytes to Spin Ice. 2015, 191.
(45) Ramírez, P.; Rapp, H. J.; Reichle, S.; Strathmann, H.; Mafé, S. Current-Voltage Curves of Bipolar Membranes. *J. Appl. Phys.* **1992**, *72*, 259−264.
(46) Hurwitz, H. D.; Dibiani, R. Experimental and Theoretical Investigations of Steady and Transient States in Systems of Ion Exchange Bipolar Membranes. *J. Memb. Sci.* **2004**, *228*, 17−43.
(47) Newman, J.; Thomas-Alyea, K. E. *Electrochemical Systems*, 3rd ed.; John Wiley and Sons, Inc.: Hoboken, NJ, 2004.
(48) Onsager, L.; Fuoss, R. M. Irreversible Processes in Electrolytes. Diffusion, Conductance, and Viscous Flow in Arbitrary Mixtures of Strong Electrolytes. *J. Phys. Chem.* **1932**, *36*, 2689−2778.
(49) Divekar, A. G.; Park, A. M.; Owczarczyk, Z. R.; Seifert, S.; Pivovar, B. S.; Herring, A. M. A Study of Carbonate Formation Kinetics and Morphological Effects Observed on OH - Form of Pfaem When Exposed to Air Containing CO 2. *ECS Trans.* **2017**, *80*, 1005−1011.
(50) Berlinger, S. A.; McCloskey, B. D.; Weber, A. Z. Inherent Acidity of Perfluorosulfonic Acid Ionomer Dispersions and Implications for Ink Aggregation. *J. Phys. Chem. B* **2018**, *122*, 7790−7796.
(51) Spry, D. B.; Fayer, M. D. Proton Transfer and Proton Concentrations in Protonated Nafion Fuel Cell Membranes. *J. Phys. Chem. B* **2009**, *113*, 10210−10221.
(52) Sondheimer, S. J.; Bunce, N. J.; Lemke, M. E.; Fyfe, C. A. Acidity and Catalytic Activity of Nafion-H. *Macromolecules* **1986**, *19*, 339−343.
(53) Weng, L. C.; Bell, A. T.; Weber, A. Z. Towards Membrane-Electrode Assembly Systems for CO2 Reduction: A Modeling Study. *Energy Environ. Sci.* **2019**, *12*, 1950−1968.
(54) Ehlinger, V. M.; Crothers, A. R.; Kusoglu, A.; Weber, A. Z. Modeling Proton-Exchange-Membrane Fuel Cell Performance/Degradation Tradeoffs with Chemical Scavengers. *J. Phys. Energy* **2020**, DOI: 10.1088/2515-7655/abb194. *in press*
(55) Grew, K. N.; Chiu, W. K. S. A Dusty Fluid Model for Predicting Hydroxyl Anion Conductivity in Alkaline Anion Exchange Membranes. *J. Electrochem. Soc.* **2010**, *157*, B327.
(56) Grew, K. N.; Ren, X.; Chu, D. Effects of Temperature and Carbon Dioxide on Anion Exchange Membrane Conductivity. *Electrochem. Solid-State Lett.* **2011**, *14*, 5−10.
(57) Choi, P.; Jalani, N. H.; Datta, R. Thermodynamics and Proton Transport in Nafion II. Proton Diffusion Mechanisms and Conductivity. *J. Electrochem. Soc.* **2005**, *152*, E123.
(58) Natzle, W. C.; Moore, C. B. Recombination of Hydrogen Ion (H+) and Hydroxide in Pure Liquid Water. *J. Phys. Chem.* **1985**, *89*, 2605−2612.
(59) Critchfield, F. E.; Gibson, J. A.; Hall, J. L. Dielectric Constant for the Dioxane-Water System from 20 to 35°. *J. Am. Chem. Soc.* **1953**, *75*, 1991−1992.
(60) Peng, J.; Roy, A. L.; Greenbaum, S. G.; Zawodzinski, T. A. Effect of CO_2 Absorption on Ion and Water Mobility in an Anion Exchange Membrane. *J. Power Sources* **2018**, *380*, 64−75.
(61) Weber, A. Z.; Newman, J. Transport in Polymer-Electrolyte Membranes. *J. Electrochem. Soc.* **2004**, *151*, A311.
(62) Resasco, J.; Lum, Y.; Clark, E.; Zeledon, J. Z.; Bell, A. T. Effects of Anion Identity and Concentration on Electrochemical Reduction of CO2. *ChemElectroChem* **2018**, *5*, 1064−1072.
(63) Larrazábal, G. O.; Strøm-Hansen, P.; Heli, J. P.; Zeiter, K.; Therkildsen, K. T.; Chorkendorff, I.; Seger, B. Analysis of Mass Flows and Membrane Cross-over in CO2 Reduction at High Current Densities in an MEA-Type Electrolyzer. *ACS Appl. Mater. Interfaces* **2019**, *11*, 41281−41288.
(64) Sankir, M.; Kim, Y. S.; Pivovar, B. S.; McGrath, J. E. Proton Exchange Membrane for DMFC and H2/Air Fuel Cells: Synthesis and Characterization of Partially Fluorinated Disulfonated Poly(Arylene Ether Benzonitrile) Copolymers. *J. Memb. Sci.* **2007**, *299*, 8−18.
(65) Wilhelm, F. G. *Bipolar Membrane Electrodialysis - Membrane Development and Transport Characteristics*; 2001.
(66) Balster, J.; Stamatialis, D. F.; Wessling, M. Electro-Catalytic Membrane Reactors and the Development of Bipolar Membrane Technology. *Chem. Eng. Process. Process Intensif.* **2004**, *43*, 1115−1127.
(67) Kushner, D. I.; Crothers, A. R.; Kusoglu, A.; Weber, A. Z. Transport Phenomena in Flow Battery Ion-Conducting Membranes. *Curr. Opin. Electrochem.* **2020**, *21*, 132−139.
(68) Kreuer, K. D.; Paddison, S. J.; Spohr, E.; Schuster, M. Transport in Proton Conductors for Fuel-Cell Applications: Simulations, Elementary Reactions, and Phenomenology. *Chem. Rev.* **2004**, *104*, 4637−4678.
(69) Kreuer, K. D. The Role of Internal Pressure for the Hydration and Transport Properties of Ionomers and Polyelectrolytes. *Solid State Ionics* **2013**, *252*, 93−101.

https://dx.doi.org/10.1021/acsami.0c12686
ACS Appl. Mater. Interfaces 2020, 12, 52509−52526